



**KTH Industrial Engineering  
and Management**

# **??THEORETICAL STUDY OF CU-BASED QUATERNARY CHALCOGENIDE SEMICONDUCTORS??**

RONGZHEN CHEN

Licentiate Thesis

School of Industrial Engineering and Management, Department of  
Materials Science and Engineering, KTH, Sweden, 2014

ISRN KTH/MSE-12/09-SE+AMFY/AVH  
ISBN 978-91-7501-313-8

Materialvetenskap  
KTH  
SE-100 44 Stockholm  
Sweden

Akademisk avhandling som med tillstånd av Kungliga Tekniska Högskolan framlägges till offentlig granskning för avläggande av **???licentiatexamen fredagen den 23 Nov. 2014 kl 10:00 i koenferencerum???**, Materialvetenskap, Kungliga Tekniska Högskolan, Brinellvägen 23, Stockholm.

© Rongzhen Chen, 2014

Tryck: Universitetsservice US AB

## Abstract

In order to reduce the high dependence on fossil fuels and oil, solar energy is one of the alternatives. Thin film photovoltaic (PV) technology is one of the solar energy, and there are several rather important absorber materials in the PV technology, such as the cadmium telluride (CdTe) and chalcopyrite copper indium gallium diselenide (CIGS). The maximum conversion efficiency of CIGS had reached 23.3% in the National Renewable Energy Laboratory, Golden, Colorado, U.S.A. Therefore, the accurate information for this kind of absorber materials is of great importance in order to design the photovoltaic materials.

In the licentiate thesis, two researches are investigated for CIGS. (1) Parameterization of the band dispersion for the uppermost three valence bands (VBs) and the lowest conduction band (CB) for  $\text{CuInSe}_2$ ,  $\text{CuIn}_{0.5}\text{Ga}_{0.5}\text{Se}_2$ , and  $\text{CuGaSe}_2$  is modeled, which is based on the  $\mathbf{k} \cdot \mathbf{p}$  method, but extended it up to high order. It demonstrates that the VBs and CB are quite non-parabolic away from the  $\Gamma$  point, which implies that the effective mass on  $\Gamma$  point is not suitable to describe the materials properties such as band filling and strong excitation effects. (2) The dielectric function spectra of  $\text{CuIn}_{0.5}\text{Ga}_{0.5}\text{Se}_2$  is calculated. It is compared with the experiment result based on  $\text{CuIn}_{0.7}\text{Ga}_{0.3}\text{Se}_2$  at 40 K and 300 K, which demonstrates that the overall shape of dielectric function spectra is in good agreement for both of calculation and experiment.

Three uppermost VBs and the lowest CB of CIGS are parameterized in order to better understand and describe the anisotropy and non-parabolic of the energy dispersion. In order to illustrate the non-parabolic of the band dispersion, the effective electron and hole mass tensors are obtained in four symmetry directions. To further illustrate the non-parabolic, the constant energy surface are calculated for the three topmost VBs as well as the lowest CB. The density-of-states (DOS), Fermi energy and the carrier concentrations are calculated and analyzed based on this parameterization as well. The results are compared with the parabolic band energy approximation.

The dielectric function spectra of  $\text{CuIn}_{0.5}\text{Ga}_{0.5}\text{Se}_2$  is determined by the all electron and full-potential linearized augmented plane wave calculations (FPLAPW). It shows a good agreement with the result from spectroscopic ellipsometry, which illustrates the results of  $\text{CuIn}_{0.7}\text{Ga}_{0.3}\text{Se}_2$  at 40 K and 300 K. Furthermore, the probable electronic origins of observed interband critical points are discussed. The band to band analysis of the contribution to the total imaginary part of dielectric function spectrum is explored as well.

## Preface

### List of included publications:

- I Parameterization of  $\text{CuIn}_{1-x}\text{Ga}_x\text{Se}_2$  ( $x = 0, 0.5$ , and  $1$ ) energy bands  
R. Chen and C. Persson, *Thin Solid Films* **519**, 7503 (2011).
- II Band-edge density-of-states and carrier concentrations in intrinsic and *p*-type  $\text{CuIn}_{1-x}\text{Ga}_x\text{Se}_2$   
R. Chen and C. Persson, *J. Appl. Phys.* **112**, 103708 (2012).
- III Dielectric function spectra at 40 K and critical-point energies for  $\text{CuIn}_{0.7}\text{Ga}_{0.3}\text{Se}_2$   
S.G. Choi, R. Chen, C. Persson, T.J. Kim, S.Y. Hwang, Y. D. Kim, and L. M. Mansfield, *Appl. Phys. Lett.* **101**, 261903 (2012).

### My contribution to the publications:

- Paper I:** modeling, analysis of result, literature survey; the manuscript was written jointly.
- Paper II:** modeling, analysis of result, literature survey; main part of the manuscript was written.
- Paper III:** all calculations, analysis of the theoretical part, part of literature survey; the manuscript was written jointly.

### Publications not included in the thesis:

#### Book chapter:

- IV Electronic structure and optical properties from first-principles modeling  
C. Persson, R. Chen, H. Zhao, M. Kumar, and D. Huang, Chapter in "Copper zinc tin sulphide-based thin film solar cells", edited by K. Ito (John Wiley & Sons, ??Hoboken??, 2014).

#### International conference contributions:

- V Band structure and optical properties of  $\text{CuInSe}_2$   
R. Chen and C. Persson, *Advanced Materials Research Journal* **894**, 254 (2014).  
*4th Int. Conf. on Adv. Mater. Res (ICAMR-4), Macao, China, 23–24 Jan. 2014.*
- VI Electronic modeling and optical properties of  $\text{CuIn}_{0.5}\text{Ga}_{0.5}\text{Se}_2$  thin film solar cell  
R. Chen and C. Persson, *J. Appl. Math. & Phys.* **2**, 41 (2014).  
*Conf. on New Adv. Cond. Matter Phys. (NACMP 2014), Shenzhen, 14–16 Jan 2014.*

# Contents

Preface	v
Contents	vii
<b>1 Introduction</b>	<b>1</b>
1.1 Solar cells . . . . .	3
1.1.1 Single-junction solar cells . . . . .	3
1.2 Solar cell materials . . . . .	8
1.2.1 Crystalline silicon solar cells . . . . .	9
1.2.2 Gallium arsenide . . . . .	10
1.2.3 Thin film materials . . . . .	10
1.3 Copper indium gallium diselenide (CIGS) materials . . . . .	11
1.3.1 Crystal structure . . . . .	11
1.3.2 Optical properties and defects in the CIGS . . . . .	12
1.3.3 CIGS solar cell structure . . . . .	13
<b>2 Theory</b>	<b>15</b>
2.1 Electronic structure calculations . . . . .	15
2.1.1 The quantum many-body problem . . . . .	15
2.1.2 The Born-Oppenheimer approximation . . . . .	16
2.1.3 Hartree, Hartree-Fock approximation and density functional theory	18
2.1.3.1 Hartree approximation . . . . .	18
2.1.3.2 Hartree-Fock approximation . . . . .	21
2.1.3.3 Density functional theory . . . . .	22
2.1.3.4 Kohn-Sham equation . . . . .	24
2.1.3.5 The exchange-correlation potential . . . . .	26
2.1.4 Solving the secular equation . . . . .	27
2.1.5 Eigenvalue problem . . . . .	29
2.2 Full-potential linearized augmented plane wave method . . . . .	30
2.2.1 Introduction . . . . .	30
2.2.2 Wavefunction . . . . .	31
2.2.2.1 Augmented plane wave method . . . . .	31
2.2.2.2 Linearized augmented plane wave method . . . . .	32

2.2.2.3	Linearized augmented plane wave method plus local orbitals . . . . .	33
2.2.2.4	Augmented plane wave method plus local orbitals . . . . .	33
2.2.3	Effective potential . . . . .	34
2.3	Dielectric function . . . . .	34
2.4	$k \cdot p$ method . . . . .	35
2.5	Spin-orbit coupling . . . . .	36
2.5.1	Dirac equation . . . . .	36
2.5.2	Derivation of spin-orbit coupling . . . . .	37
<b>3</b>	<b>Results and discussion</b>	<b>40</b>
3.1	Parameterization of energy bands for CIGS . . . . .	40
3.1.1	Parameterization method . . . . .	40
3.1.2	Non-parabolicity properties . . . . .	42
3.1.3	Application of the full band parameterization . . . . .	46
3.2	Dielectric function for $\text{CuIn}_{0.5}\text{Ga}_{0.5}\text{Se}_2$ . . . . .	53
<b>4</b>	<b>Summary of the publications</b>	<b>56</b>
<b>5</b>	<b>Concluding remarks and future work</b>	<b>58</b>
<b>Acknowledgements</b>		<b>59</b>
<b>Bibliography</b>		<b>60</b>

# Chapter 1

## Introduction

With the increasing of energy consumption, more and more energy or power is needed. According to the statistical review of world energy on 2014 [1] (**Fig. 1.1**), the required energy is mainly satisfied by the fossil fuels (mainly coal, petroleum and natural gas), with a market share of around 87%. The total energy consumption is between 12000 and 13000 million tonnes oil equivalent (MTOE), which is equivalent to around 15 terawatts. Normally light bulbs in our homes consume around 50 to 100 watts of energy, 1 terawatt implies 10 billion of the 100 watts light bulbs are lighted at the same time. Unfortunately, the fossil fuels is very limited energy and non-renewable resources, one day which is not far from now it will be dissipated due to the energy consumption growth.

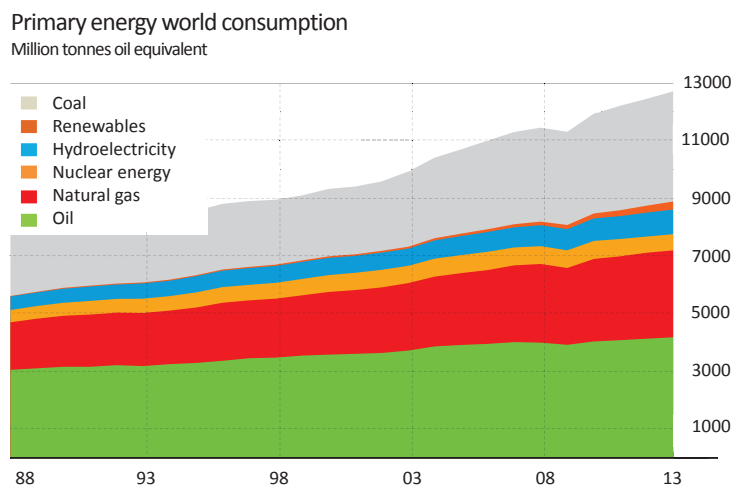


**Figure 1.1.** Data is from BP statistical review of world energy 2014 [1].

By the year of 2050, the total world energy consumption will double [2]. Therefore, it is urgent to explore more sustainable and environmentally friendly energy sources. In **Fig. 1.1**, renewable energy (mainly solar energy, wind power, and geothermal energy)

in 2014 accounts for around 2% of energy consumption globally. It is important to focus on the renewable energy research from a long term point of view. The solar energy technologies are one of the hot topic among the renewable energy research considering the point of CO<sub>2</sub> free, reliable energy supply, no cooling water requirement and operation in silence.

The solar energy technologies are the way to produce electricity from the light of the sun. Sunlight is a portion of the radiation by the sun, like ultraviolet, visible, and infrared light. The spectrum of the sun is close to the spectrum of black body with a temperature of about 6000 K (Fig. 1.2). In the field of photovoltaics (PV), solar spectrum is established by air mass (AM) which defines the direct optical path length through the Earth's atmosphere [3]. The AM1.5 and AM0 are important: AM1.5 is the air mass at a solar zenith angle of 48.19 degree, and AM0 mean the solar spectrum outside of the atmosphere. Generally, solar spectrum at AM1.5 is used in PV field in order to standardize solar cell measurements. In Fig. 1.2, the absorption in the atmosphere is quite strong by gases, dust and aerosols, as well as the scattering of light from air molecules [4].

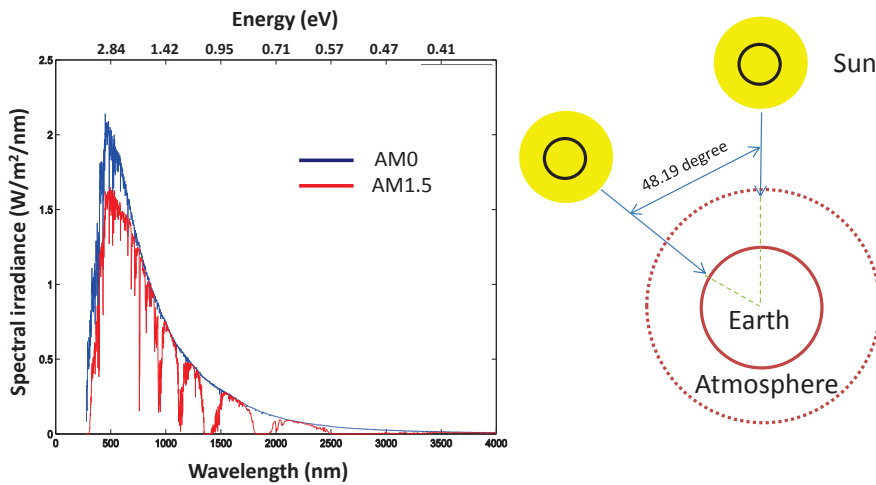


**Figure 1.2.** Spectral irradiance AM1.5 and AM0.

There are mainly three kinds of solar energy technologies [5, 6]. The first one is solar thermal, which utilizes the flat sunlight collector plates to harness the energy from sunlight to heat water for use in industries, homes, and pools. Therefore, the solar thermal collectors do not convert sunlight to electricity directly, but transfer the energy to heat up the water instead. The advantage is the conversion efficiency is relatively higher. The second one is solar chemical, which takes advantage of solar energy by absorbing sunlight in a chemical reaction. However, the conversion efficiency is quite low. The last one is solar photovoltaics (solar cell), which is the way to utilize solar panels to convert sunlight into electricity. The installation is easier, occupy less space and less maintenance compared with solar thermal. The conversion efficiency is higher than

solar chemical. However, all the three solar energy technologies are environmentally friendly.

## 1.1 Solar cells

In the worldwide, the conversion efficiencies in all different types of solar cells are improved remarkably [7]. From Fig. 1.3, the highest efficiency for multijunction cells, crystalline silicon cells, thin-film technologies and new emerging cells are around 44.7%, 27.6%, 23.3% and 17.9% (19.3% by Yang Yang Laboratory team at University of California, May 2014 [ [8]]), respectively. Therefore, the solar cell is a very important and promising way to produce the renewable energy.

Multijunction cells are the cells which contain multi *p-n* junctions (or subcells) which have different band-gap for each *p-n* junction. Therefore, different wavelengths of light from the Sun are absorbed for each of junction. For example, wider band-gap junction is at the front of the cell, which can absorb the photons with high energy; the junction with low band-gap can absorb the photons with relatively low energy. Therefore, the conversion efficiency is higher than single *p-n* junction, for example, the maximum conversion efficiency is 44.7% by Soitec [9] using four-junction or more in Fig. 1.3. Crystalline silicon cells are the most widely utilized in the photovoltaic industries, which built the solar cells using crystalline silicon (c-Si). It has two types in the crystalline silicon photovoltaics: mono-crystalline silicon and multi-crystalline silicon. The crystalline silicon cells have high efficiency, for example, the maximum conversion efficiency is 27.6% with concentrator by Amonix [10] and maximum 25.6% without concentrator by Panasonic [11] in Fig. 1.3. Thin-Film solar cells are the cells which are made by depositing one or several thin layers, which allows the cells to be rather flexible and resulting in lower weight. The maximum conversion efficiency is lower than crystalline silicon today, which has the maximum conversion efficiency 23.3% using CIGS with concentrator by NREL [12] and 21.7% without concentrator by the center for solar energy and hydrogen research (ZSW) in Stuttgart [13] in Fig. 1.3. The Emerging PV in Fig. 1.3 represents the newest ways to create electricity from sunlight and potentially with higher conversion efficiency, such as perovskite cells. The maximum conversion efficiency of perovskite cells already reached 19.3% by the group Yang Yang at the University of California, Los Angeles [8]. Perovskite cells jump into the world of solar cells only in 2009 [14, 15], and the conversion efficiency is improved remarkable within 5 years. Certainly, the search and optimization of alternatively solar cell materials is still an ongoing and active area today.

### 1.1.1 Single-junction solar cells

The *p-n* junction is the fundamental building block of solar cells. The single *p-n* homojunction will be explored in this section. The more detailed information can be found from Refs. [16–18].

# Best Research-Cell Efficiencies

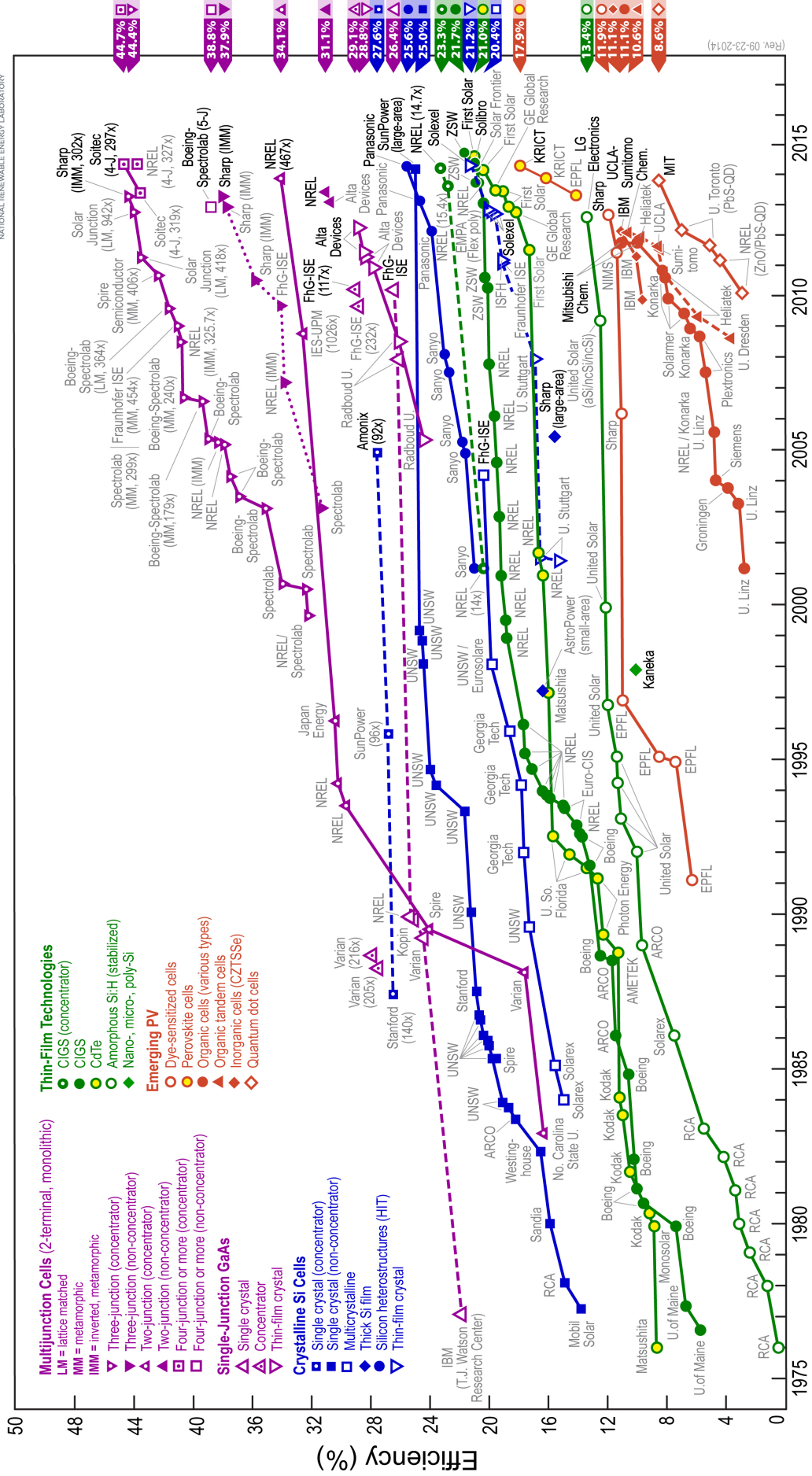
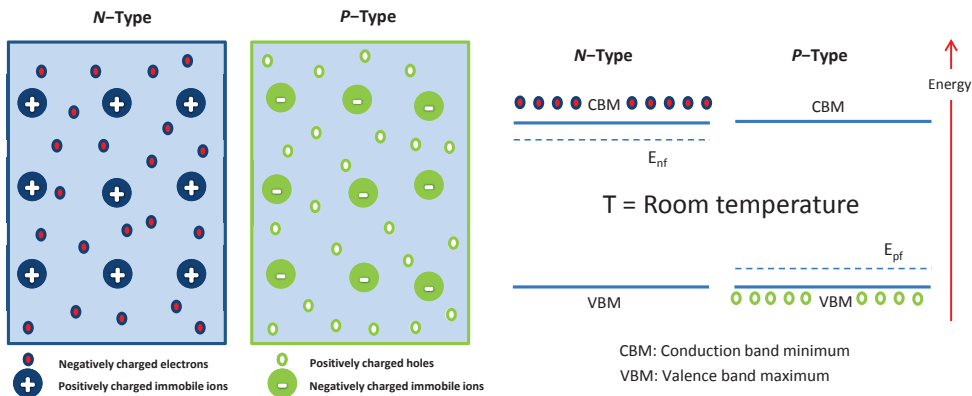


Figure 1.3. Best research-cell efficiencies. Figure is from National Renewable Energy Laboratory (NREL), Golden, Colorado, U.S.A.

We start from the separate *n*-type material and *p*-type material at room temperature (assume that all the donor (acceptor) atoms are positively (negatively) ionized at room temperature). In Fig. 1.4, the left panel shows the separated *n*-type and *p*-type materials. The *n*-type material has many free negatively charged electrons which can move freely inside the material, and there are numbers of positively charged immobile donor ions as well. Similarly, the *p*-type material has many free positively charged holes which can move freely in the material, and there are numbers of negatively charged immobile acceptor ions as well. However, the material is still neutral in both *n*-type and *p*-type. The corresponding Fermi levels are shown on the right panel. The Fermi level ( $E_{nf}$ ) is closer to conduction band minimum for *n*-type material due to the many free negatively charged electrons. Conversely, the Fermi level of *p*-type material ( $E_{pf}$ ) is closer to the valence band maximum to the free positively charged holes.



**Figure 1.4.** Left panel: Doped (*n*-type and *p*-type) materials in dark at room temperature. Right panel: Energy band diagram of separated *p*-*n* homojunction in dark at room temperature for two-level model. Assume that all the donor (acceptor) atoms are positively (negatively) ionized at room temperature.

If the *n*-type and *p*-type materials are joined, the free electrons (holes) in *n*-type (*p*-type) material will diffuse into *p*-type (*n*-type) material due to the lower concentrations of electrons (holes) in the *p*-type material (Fig. 1.5). In the region which is near the interface between *n*-type and *p*-type materials, the ionized donor and acceptor ions create a "build in" electric field which points from the *n*-type material to the *p*-type material. This causes the drift of carriers in the opposite direction. The "build-in" electric field forces the electrons (holes) back into the *n*-type (*p*-type). At certain point, the whole material can reach a stable equilibrium due to the achieved balance between diffusion and drift. Formation of the "build-in" electric field is rather important for the solar cells, even though there is no current in the material so far. In the following text, the region which forms the "build-in" electric field is also called space charge region (SCR). The different Fermi levels for *n*-type and *p*-type materials are equal at the stable equilibrium.

Therefore, the energy bands bend over and create a potential barrier near the junction (right panel in **Fig. 1.5**). Finally, there is a internal potential  $V_{bi}$  in the junction, which can block the diffusion.

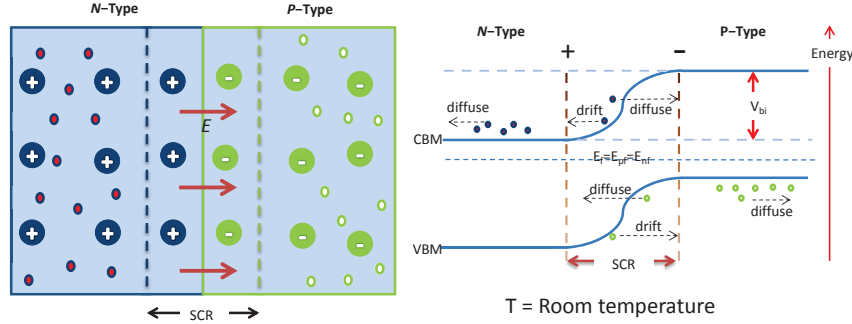


**Figure 1.5.** Left panel: The *p-n* homojunction in dark at room temperature. Right panel: Energy band diagram of *p-n* homejunction at the equilibrium in dark at room temperature for two-level model.

The *p-n* junction cell with and without the illumination are discussed in **Fig. 1.6** and **Fig. 1.7**. If there was a wire with certain resistance connecting the *n*-type and *p*-type, there is no current in the wire under the condition of dark (no illumination). However, if the light shines on the cell or component, a current can be generated from the *p*-type to the *n*-type side (conventional current). Because the electrons from valence bands (VBs) goes to conduction bands (CBs), which can generate pairs of electron-hole. At the same time, the recombination of paired electron-hole occurs. The rate of generation is faster than that of recombination. Therefore, net generation occurs. Apparently, there are three regions in the whole junction cell where the electrons goes from VBs to CBs, the *n*-type region, the *p-n* junction, and the *p*-type region. In the either *n*-type or *p*-type region (especially, region which is far away SCR), the electron-hole pairs can not remain long time, it is most probable that electrons will jump down from CBs to VBs again. However, the electron-hole pairs can be separated in the *p-n* junction region due to the "build-in" electric field. Therefore, the current is generated. Actually, the electron-hole pairs in the either *n*-type and *p*-type (especially, for them which are near SCR) also have the chance to diffuse into the SCR, which can contribute the generation of current or reduce the current as well.

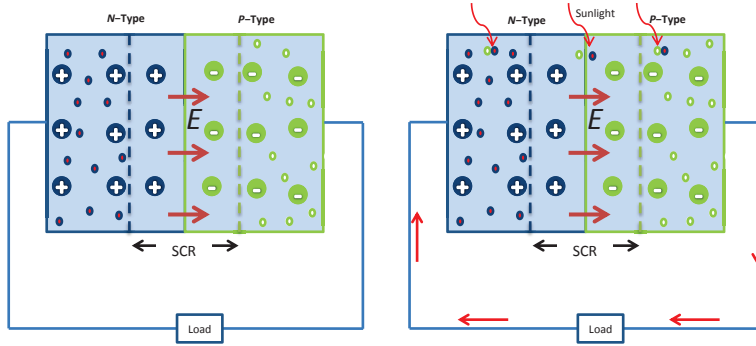


**Figure 1.6.** Left panel: the  $p$ - $n$  homojunction at dark with load. Right panel: the  $p$ - $n$  homojunction under illumination with load at room temperature for two-level model.

In Fig. 1.7, the SCR becomes more "smooth" due to the extra load, such as light bulb. It is equivalent to apply external potential. The stabilized Fermi level at the stable equilibrium splits under illumination. The chemical potential  $\nabla\mu$  ( $E_{nf} - E_{vf}$ ) is created, which is considered as the electron charge times the voltage across the device. The generation and recombination by impurities are not analyzed in here.

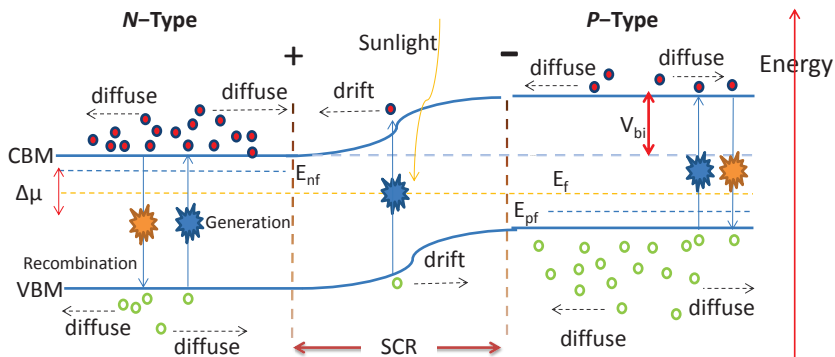


**Figure 1.7.** Energy band diagram of a  $p$ - $n$  homojunction under illumination with load.

The current-voltage characteristics is defined in Fig. 1.8 with some important parameters of the solar cells. The  $V_{oc}$  and  $I_{sc}$  are the open circuit voltage and short circuit current, respectively. They are the maximum voltage and maximum current from the solar cells. The  $V_{mp}$  and  $I_{mp}$  are the voltage and current which yields the maximum power. The maximum power generated by the solar cells is  $P_{out} = V_{mp} \times I_{mp}$ . That is the rectangle bounded by the dashed lines in Fig. 1.8.

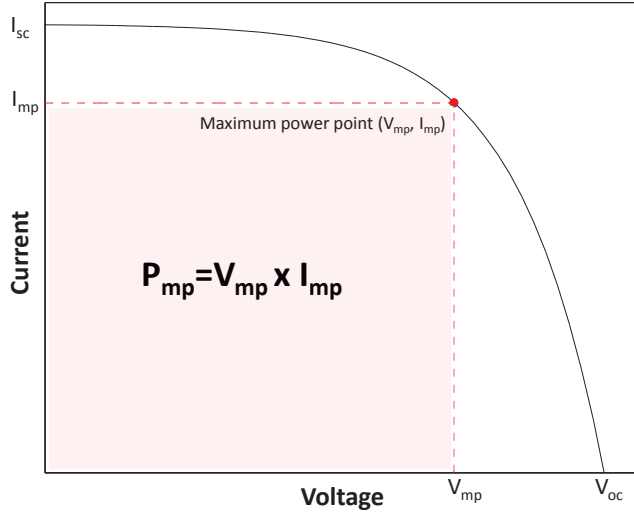


**Figure 1.8.** Current-voltage characteristics of a solar cell under illumination.

The fill factor ( $FF$ ) and the power conversion efficiency ( $\eta$ ) are often represented the solar cell performance

$$FF = \frac{P_{out}}{V_{oc} \cdot I_{sc}} = \frac{V_{mp} \cdot I_{mp}}{V_{oc} \cdot I_{sc}} \quad (1.1)$$

$$\eta = \frac{P_{out}}{P_{in}} = \frac{FF \cdot V_{oc} \cdot I_{sc}}{P_{in}}. \quad (1.2)$$

Here,  $P_{in}$  is the incident photon power per second. The conversion efficiency of the solar cells is proportional to  $FF$ ,  $V_{oc}$ , and  $I_{sc}$ . There are several aspects which can affect the conversion efficiency.  $V_{oc}$  is directly proportional to the band-gap of the material,  $I_{sc}$  is proportional to the number of absorbed photons. When the band-gap is decreased, the more of the spectrum is absorbed. However, the  $V_{oc}$  will be reduced in this case. More importantly, the excess energy of photons is lost due to the thermalization in the cells. When the band-gap is increased, transparency losses from the photons with energy lower than band-gap. There is more detailed analysis of conversion efficiency in the Ref. [16].

## 1.2 Solar cell materials

In 1839, the French physicist A. E. Becquerel [19] revealed the photovoltaic effect for the first time. Charles Fritts built the first solid state photovoltaic (PV) cell using semiconductor selenium in 1883 [20, 21]. It is not until 1941 that the first silicon-based solar cell was demonstrated [22, 23]. Today, there are many different types of solar cell materials. The reason why the best solar cell material is not realized yet is that it is expected to be

not only high efficiency but also environmentally friendly and low cost. It requires not only that the growth and manufacturing process of solar cell materials shall be cheaper, but also that the devices shall have longer application life. Moreover the raw material should be abundant and non-toxic as well. In this section, four main solar cell materials are discussed briefly: silicon (Si), gallium arsenide (GaAs), cadmium telluride (CdTe), copper indium gallium diselenide (CIGS).

Potential solar cell materials need to fulfill several properties, such as large absorption coefficient and a band-gap energy between 0.7 to 2.0 eV. Under these conditions, there are quite many materials satisfying the requirements. However, some other properties are needed to be considered as well, such as cost and environmental safety. Thereby, only part of them are suitable to produce in reality.

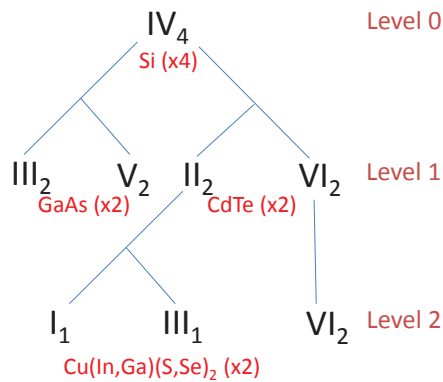


**Figure 1.9.** Tree of tetragonal bonded semiconductor, the roman numerals mean the group numbers in the chemical element periodic table, and the subscript implies the number of elements.

In Fig. 1.9, the formation of tetragonal semiconductors is considered as a series of cation mutations where the total number valence electrons is the same and keep the charge neutral [24–26]. For example, group number IV element Si (level 0) with four 4<sup>+</sup> ions is equivalent to two 3<sup>+</sup> ions and two 5<sup>+</sup> ions, such as GaAs (level 1). It is also equivalent to two 2<sup>+</sup> ions and two 6<sup>+</sup> ions, such as CdTe (level 1). The CIGS can be generated applying the same process on II element on the level 1 in Fig. 1.9. This method was suggested by Goodman and Pamplin [27,28].

### 1.2.1 Crystalline silicon solar cells

The solar cell based on Si dominates the solar power world today, which accounts for more than 90% of the total PV market [29]. This kind of solar cell takes advantage of different forms of Si, that is, monocrystalline Si and polycrystalline Si. The success of Si is due to a number of reasons. Over 90% in the crust of earth is composed of silicate minerals, which yields huge available Si. Moreover, it has higher conversion efficiency,

and it is also proved that it has excellent stability and reliability under the outdoor condition. However, Si also have drawbacks. It has an indirect band-gap and hence it has a lower optical absorption coefficient. In order to absorb the incident sunlight fully, it requires to thicker Si (wafer) (around 0.2 mm) to absorb the sunlight [30]. Crystalline Si have to be high quality and defect free in order to avoid to lost the carriers before collection. Last but not least, it is expensive to purify the Si from silicate minerals, which really limits the cost reduction potential of wafer-based Si technology.

However, the solar cells based crystalline Si technology is still leading the market of solar cell since many companies are trying to lower the cost of the whole process.

### 1.2.2 Gallium arsenide

GaAs has a zinc blende crystal structure with a direct band-gap around 1.5 eV at room temperature [31–33]. Some electronic properties of GaAs are superior to Si, such as higher electron mobility, higher saturated electron velocity, absorb sunlight more efficiently due to the direct band-gap. The optimum band-gap for the single junction solar cell is suggested around 1.3 eV by theoretical calculation from Henry (1980) [34] who modified the original Shockley-Queisser limit [35]. Therefore one of the most applications of GaAs is solar cells. GaAs has been extensively researched since the 1950s, and the first GaAs solar cells were established in 1970 by the Zhores Alferov's team [36]. Today, the conversion efficiency for single function solar cell based on GaAs is around 28.8% [37]. However, it is more difficult to grow and the solar cell component has higher price in comparison with Si. Researches are focusing on how to reduce the price today, and the main application solar cell based on GaAs is in the space application. However, the arsenic toxicity should be considered.

The conversion efficiency for four-junction GaInP/GaAs//GaInAsP/GaInAs concentrator solar cells is reached 44.7% by Soitec on March 2014 [9].

### 1.2.3 Thin film materials

Thin film solar cells have several thin films with the total thickness less than 10  $\mu\text{m}$  [38]. The cost can potentially be lower since the less materials are utilized to make thin film solar cells. The development of thin film solar cell was started since 1970s. Currently, the maximum conversion efficiency for thin film is 23.3% [12]. Three different thin film materials are discussed in this section: amorphous silicon (a-Si), cadmium telluride (CdTe), and copper indium gallium diselenide (CIGS).

A-Si solar cells are the first thin film solar cell material which reach the large-scale production [39–41]. It has higher absorption coefficient than crystalline Si. Therefore, the thickness can be less than 1  $\mu\text{m}$ . The main disadvantages a-Si solar cells is the lower efficiency, the actual conversion efficiency for the commercial single junction solar cells based on a-Si is between 4% to 8% [42]. This limits the development of a-Si thin film

solar cells. A-Si solar cells are suited to the situation which requires low cost over high efficiency.

CdTe was first reported in the 1960s [43]. However, it is not developed rapidly until in the early 1990s. CdTe has a number of advantages as an absorber. It has higher absorption coefficient. The band-gap is around 1.45 eV, which is very near the optimum value for single-junction solar cells. The manufacturing process is easier to control, which results in the cost of manufacturing is low [44]. Moreover, the commercial modules already reach the efficiency of 16%. However, an important question is needed to be considered in order to large-scale CdTe manufacturing: cadmium toxicity and tellurium availability.

CIGS are direct band-gap semiconductors with high optical absorption coefficients. It is seen as one of the most promising solar cell material for the near future. It is always employed in a heterojunction structure, mainly it is with the thinner *n*-type CdS layer [45]. The conversion efficiency of CIGS reached up to 20% in the laboratory cell [46]. The interesting part is that it can be alloyed by the ratio of Ga/(Ga+In), and the band-gap can be tuned along with that. The band-gap is between 1.0 eV to 1.7 eV for this alloy [47–51]. CIGS does not contain any toxic element.

## 1.3 Copper indium gallium diselenide (CIGS) materials

CIGS material is a chalcopyrite-type material, which is considered to be one of the most promising thin film solar cell material. The direct band-gap is from around 1.0 eV to 1.7 eV by alloying Ga in the CuInSe<sub>2</sub> (CIS), and the conversion efficiency in laboratory already surpassed 20%. CuInSe<sub>2</sub> was first synthesized by Hahn in 1953 [52]. It was first exploited as an absorber material in a single crystal solar cell in 1974 [53], which is based on CuInSe<sub>2</sub> and CdS. The conversion efficiency is around 5%. The first thin film solar cells based on CuInSe<sub>2</sub> and CdS was invented by Kazmerski. During 1980s, Boeing Corporation did much research on the thin film polycrystalline CIGS solar cells. To date, the highest conversion efficiency in lab situation for the solar cells based on CIGS is 23.3% [12].

### 1.3.1 Crystal structure

The crystal structure of CIGS can be derived from the zinc blende crystal structure of zinc selenide (ZnSe). In Fig. 1.10, the crystal structures of ZnSe and CuInSe<sub>2</sub> are presented. The elements Zn are replaced by Cu and In or Ga elements in the zinc blende of ZnSe. It requires to double the unit cell in the *z*-direction. Because the bond strength and lengths between Cu-Se and In-Se or Ga-Se are different. Therefore, the lattice parameter *c* is not exact  $2a$  normally [25].

Chalcopyrite CuInSe<sub>2</sub> and CuGaSe<sub>2</sub> have the space group  $D_{2d}^{12}$  ( $I\bar{4}2d$ ; space group no. 122). The conventional unit cell has four copper atoms on the Wyckoff positions  $4a$ , four

indium/gallium atoms on position  $4b$ , and eight selenium atoms on the  $8d$  position. The cation positions have all  $S_4$  point-group symmetry, and Se have  $C_2$  symmetry. The Se  $8d$  position is fully defined with the position  $(x, y, z)$ , and each anion Se-atom has two inequivalent bonds  $\delta X\text{-Se}$  to the cations  $X = \text{Cu}$  and  $\text{In/Ga}$  [54–56]. For the alloy of  $\text{CuIn}_{0.5}\text{Ga}_{0.5}\text{Se}_2$ , the structure is chosen so that each Se atom bonds to two Cu atoms, one In, and one Ga atom. The space group is  $S_4^2$  ( $I\bar{4}$ ; space group no. 82) [57].

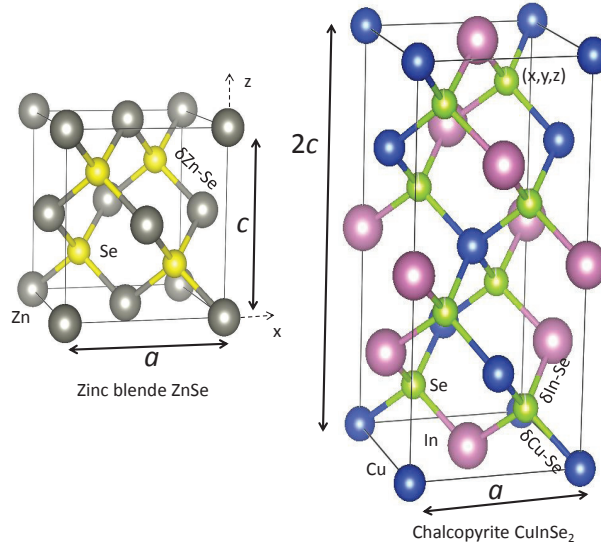


**Figure 1.10.** Crystal structures of Zinc blende ZnSe and chalcopyrite  $\text{CuInSe}_2$ .

### 1.3.2 Optical properties and defects in the CIGS

$\text{CuInSe}_2$  has a direct band-gap around 1.0 eV, and the absorption coefficient is relatively higher than Si due to direct band-gap. The quaternary CIGS alloy will be available by alloying Ga element, while the band-gap is tuned as well from 1.0 eV to 1.7 eV. The high absorption coefficient makes the CIGS material possible to be an absorber for the thin film solar cells. The band-gap can be approximated by the function of Ga content ( $x$ ) [58]

$$E_g(x) = 1.0 + 0.564x + 0.116x^2 \quad (1.3)$$

Alloying the Ga element will decrease the electron affinity of CIGS, which will make the conduction band upward shift. However, the valence band remain the same position [59]. This also explains the reason why the band-gap increases with more Ga element in the CIGS material. An overview properties of  $\text{CuInSe}_2$  and  $\text{CuGaSe}_2$  materials are described in **Table. 1.1**

Properties of CuInSe <sub>2</sub> and CuGaSe <sub>2</sub>		
Properties	CuInSe <sub>2</sub>	CuGaSe <sub>2</sub>
Space group	$D_{2d}^{12}$ (I-42d), no. 122 [33]	$D_{2d}^{12}$ (I-42d), no. 122 [33]
Lattice constants (Å)	$a = b = 5.78, c = 11.55$ [33]	$a = b = 5.61, c = 11.00$ [33]
Wyckoff positions	Cu:4a, In:4b, Se:8d [54–56]	Cu:4a, Ga:4b, Se:8d [54–56]
Direct band-gap (eV)	$E_g = 1.01$ [33]	$E_g = 1.68$ [33]
Effective masses on Γ point ( $m_0$ )	Electrons: 0.08 [60] Holes(heavy): 0.71 [60]	Electrons: 0.14 [60] Holes(heavy): 1.2 [60]
Main intrinsic defects	$n$ -type: V <sub>Se</sub> ; In <sub>Cu</sub> [61–64] $p$ -type: V <sub>Cu</sub> ; Cu <sub>In</sub> [61–64]	$n$ -type: V <sub>Se</sub> ; Ga <sub>Cu</sub> [61–64] $p$ -type: V <sub>Cu</sub> ; Cu <sub>Ga</sub> [61–64]
Crystal field splitting (eV)	0.006 [33]	−0.10 [65]
Spin-orbit splitting (eV)	0.23 [33]	0.238 [33]
Dielectric constants $\varepsilon(0)$	15.7 [33]	11.0 [60]
Melting temperature (K)	1260 [33]	1310 – 1340 [33]
Thermal expansion coefficients (1/K)	a axis: $11.23 \times 10^{-6}$ [33] c axis: $7.90 \times 10^{-6}$ [33]	a axis: $13.1 \times 10^{-6}$ [33] c axis: $5.2 \times 10^{-6}$ [33]
Thermal conductivity W/(cm × K)	0.086 [66]	0.129 [33]

**Table 1.1.** Properties of CuInSe<sub>2</sub> and CuGaSe<sub>2</sub>

CIGS is a nonstoichiometric compound with the deviations from stoichiometry in several percentage range. The high quality thin film solar cells mainly employ Cu-poor (Cu: 22.5–24.5%) high offstoichiometric CIGS absorber. V<sub>Cu</sub> is the most important native defects in CIGS due to their low formation energies. Therefore, CIGS can be grown  $p$ -type easily with the condition of Cu-poor (V<sub>Cu</sub>). There are some extrinsic divalent cation donors as well, such as Zn<sub>Cu</sub>, Cd<sub>Cu</sub> and Cl<sub>Se</sub>. The formation energy for them is relatively low for CIS and CuGaSe<sub>2</sub> (CGS). In fact, CIS is possible to be  $n$ -type material. However, CGS is not possible to be  $n$ -type under equilibrium conditions. The reason is that the low formation energy of V<sub>Cu</sub> limits the possibility of achieving electronic  $n$ -type character, especially in Ga-rich CIGS [67, 68]. It is maybe also explained why the best solar cell is with the Ga content of 30% ( $x = 0.3$ ), however, the band-gap energy of the CIGS suggests that the optimum solar cell conversion efficiency is obtained with between  $x = 0.5$  and  $x = 0.7$ .

### 1.3.3 CIGS solar cell structure

The solar cells device based on CIGS is a heterojunction device, which normally has five thin film layers with different functional properties [69–71]. A schematic of a conventional device structure is shown in Fig. 1.11

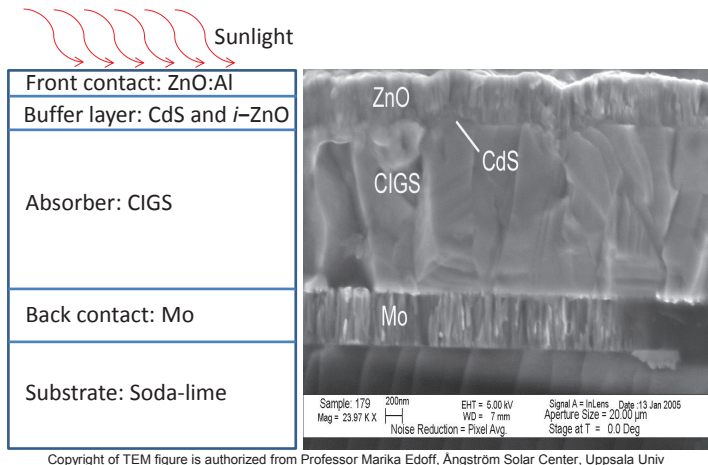


**Figure 1.11.** Structure of CIGS solar cell device, the TEM figure is from Professor Markika Edoff, Ångström Solar Center, Uppsala University[??].

Substrate is on the bottom, and there are mainly three kinds of substrates: soda-lime glass, metal and polyimide. The most common substrate is the one based on soda-lime glass containing sodium (Na) with thickness 1 mm to 3 mm. The Na will improve the efficiency and reliability of the solar cells as well as process tolerance. The molybdenum works as back contact due to its low resistivity and stability at high temperature with thickness around 500 nm. The most important part of the device is the *p*-type absorber layer: CIGS, which is doped by intrinsic defects and around 1500 – 2000 nm. The *n*-type buffer layer CdS is on the top of CIGS, which is around 60 nm. The intrinsic zinc oxide (*i*-ZnO) and *n*-type ZnO layer are followed, and it works as window layer. The *i*-ZnO is to avoid the damage of the CIGS and CdS from sputtering damage when depositing the ZnO:Al window layer, and the *n*-type ZnO is doped by the aluminum (Al) in order to get higher conductivity [72, 73]. This CIGS/CdS/ZnO structure was optimized to improve the cell performance. The detailed information about the structure CIGS solar cell device can be found in Refs. [74–76].

# Chapter 2

## Theory

### 2.1 Electronic structure calculations

#### 2.1.1 The quantum many-body problem

A solid material contains a huge number of atoms (around  $10^{23}$  cm $^{-3}$ ), and each atom consists of a nucleus surrounded by one or more electrons. According to the principles of quantum mechanics, all the properties of a system are known if one can figure out a way to solve the quantum many-body Schrödinger equation. In this thesis, the time-independent many-body Schrödinger equation is only considered, which is given as

$$H^{en}\Psi^{en}(\{\mathbf{r}_i, \mathbf{R}_I\}) = E^{en}\Psi^{en}(\{\mathbf{r}_i, \mathbf{R}_I\}). \quad (2.1)$$

Here, the superscript "en" implies that it is related with electrons and nuclei.  $\Psi^{en}(\{\mathbf{r}_i, \mathbf{R}_I\})$  is the many-particle wavefunction,  $\mathbf{r}_i$  and  $\mathbf{R}_I$  stands for coordinators of electron and nucleus.  $E^{en}$  is total energy of system.  $H^{en}$  is the Hamiltonian [77], which is defined in atomic units as

$$\begin{aligned} H^{en} = & - \sum_i^{Ne} \frac{\nabla_i^2}{2} - \sum_I^{Nn} \frac{\nabla_I^2}{2M_I} - \sum_i^{Ne} \sum_I^{Nn} \frac{Z_I}{|\mathbf{r}_i - \mathbf{R}_I|} \\ & + \frac{1}{2} \sum_i^{Ne} \sum_{j \neq i}^{Ne} \frac{1}{|\mathbf{r}_i - \mathbf{r}_j|} + \frac{1}{2} \sum_I^{Nn} \sum_{J \neq I}^{Nn} \frac{Z_I Z_J}{|\mathbf{R}_I - \mathbf{R}_J|}. \end{aligned} \quad (2.2)$$

Here, the indices  $i$  and  $j$  are used for the electrons, and  $I, J$  are used for atomic nuclei.  $Z_I$  implies the charge of the  $I$ :th nucleus.  $M_I$  is the mass of the  $I$ :th nucleus in atomic units. The first and second terms are the kinetic energy operator of the electrons and nuclei. The other terms are Coulomb interactions between electrons and nuclei, electrons and electrons and nuclei and nuclei in sequence.

**Eq. 2.1** can not be solved exactly since there are enormous number of atoms to calculate in reality. More importantly, the exact form of the wavefunction is unknown. To approximate the exact solution, one divides it into three different levels generally [77,78]: the first level is the Born-Oppenheimer approximation [79]; the second level is Hartree approximation [80], Hartree-Fock (HF) approximation [81], density functional theory (DFT) [82] and Kohn-Sham (KS) equation [83]; the last level is to solve the secular equation which is an equation that is solved to find the eigenvalue of matrix [77,78].

### 2.1.2 The Born-Oppenheimer approximation

**Eq. 2.1** should be approximated in order to solve it. A first step is to separate the wavefunction of electron and nucleus. Because the Schrödinger Hamiltonian in **Eq. 2.2** has a coupling term between the electron and nucleus, thereby one can not do that simply. The nuclei can be treated as fixed because the mass of nucleus is much larger than that of electron. This indicates that the electrons are seen as interacting under both the external potential caused by nuclei that are in fixed positions and that of the other electrons. The separation of motion between electrons and nuclei is called the Born-Oppenheimer approximation [79]. Since the positions of nuclei are fixed, wavefunction can be written as

$$\Psi^{en}(\{\mathbf{r}_i, \mathbf{R}_I\}) \approx \theta(\{\mathbf{R}_I\})\Psi(\{\mathbf{r}_i\}; \{\mathbf{R}_I\}). \quad (2.3)$$

Here,  $\Psi(\{\mathbf{r}_i\}; \{\mathbf{R}_I\})$  is the electrons wavefunction in the Born-Oppenheimer approximation. Since the electrons are under the potential of nuclei, thus the wavefunction of electrons is related with the nucleus positions.

**Eq. 2.2** can be rewritten as

$$\begin{aligned} H^{en} &= H + H^n \\ H &= U_e + U_{ext} + U_{int} \\ H^n &= -\sum_I^{Nn} \frac{\nabla_I^2}{2M_I} + U_{nn}. \end{aligned} \quad (2.4)$$

Furthermore, all the unknown terms in **Eq. 2.4** are defined as

$$\begin{aligned}
U_e &= - \sum_i^{Ne} \frac{\nabla_i^2}{2} \\
U_{ext} &= - \sum_i^{Ne} \sum_I^{Nn} \frac{Z_I}{|\mathbf{r}_i - \mathbf{R}_I|} \\
U_{int} &= \frac{1}{2} \sum_i^{Ne} \sum_{j \neq i}^{Ne} \frac{1}{|\mathbf{r}_i - \mathbf{r}_j|} \\
U_{nn} &= \frac{1}{2} \sum_I^{Nn} \sum_{J \neq I}^{Nn} \frac{Z_I Z_J}{|\mathbf{R}_I - \mathbf{R}_J|}.
\end{aligned} \tag{2.5}$$

Here,  $H$  is the Hamiltonian for the electronic system within the Born-Oppenheimer approximation. The subscript *ext* implies *external* in Eq. 2.4, and  $U_{ext}$  describes the external potentials interaction  $V_{ext}(\mathbf{r})$ .

The new Schrödinger equation combined with Eq. 2.3 and Eq. 2.4 is given as

$$(H + H^n) (\theta(\{\mathbf{R}_I\}) \Psi(\{\mathbf{r}_i\}; \{\mathbf{R}_I\})) = E^{en}(\{\mathbf{R}_I\}) (\theta(\{\mathbf{R}_I\}) \Psi(\{\mathbf{r}_i\}; \{\mathbf{R}_I\})). \tag{2.6}$$

Here,  $E^{en}(\{\mathbf{R}_I\})$  is the system total energy, which is  $\mathbf{R}_I$ -dependent because system wavefunction depends on nuclei positions. One ends up with the following equation using Eq. 2.5

$$\begin{aligned}
H\Psi(\{\mathbf{r}_i\}; \{\mathbf{R}_I\}) &= E(\{\mathbf{R}_I\})\Psi(\{\mathbf{r}_i\}; \{\mathbf{R}_I\}) \\
(U_{nn1} + U_{nn2} + U_{nn3} + U_{nn} + E(\{\mathbf{R}_I\}))\theta(\{\mathbf{R}_I\}) &= E^{en}(\{\mathbf{R}_I\})\theta(\{\mathbf{R}_I\}).
\end{aligned} \tag{2.7}$$

Here,  $E(\{\mathbf{R}_I\})$  is the total energy of electronic system, which is also  $\mathbf{R}_I$ -dependent because electrons wavefunction indirectly depends on nuclei positions. The  $U_{nn1}$ ,  $U_{nn2}$ , and  $U_{nn3}$  in Eq. 2.7 are derived as

$$\begin{aligned}
U_{nn1} &= - \sum_I^{Nn} \frac{\nabla_I^2}{2M_I} \\
U_{nn2} &= - \sum_I^{Nn} \frac{1}{M_I} \int \Psi(\{\mathbf{r}_i\}; \{\mathbf{R}_I\})^* \nabla_I \Psi(\{\mathbf{r}_i\}; \{\mathbf{R}_I\}) d\mathbf{r} \nabla_I \\
U_{nn3} &= - \sum_I^{Nn} \frac{1}{M_I} \int \Psi(\{\mathbf{r}_i\}; \{\mathbf{R}_I\})^* \nabla_I^2 \Psi(\{\mathbf{r}_i\}; \{\mathbf{R}_I\}) d\mathbf{r}.
\end{aligned} \tag{2.8}$$

In Eq. 2.7, one observes that the lattice dynamical properties of certain system within the Born-Oppenheimer approximation can be obtained. To solve this equation, the ground state energy  $E(\{\mathbf{R}_I\})$  of electronic system is needed. Here,  $\{\mathbf{R}_I\}$  are the parameterized values from the atom position.

In summary, the Schrödinger equations of the electrons and nuclei are derived separately within the Born-Oppenheimer approximation. When one refers to calculations of the ground state properties, the Schrödinger equation of the electrons is applied (the first line in Eq. 2.7). The Schrödinger equation of nuclei is employed for the calculation of lattice dynamics ( $U_{nn2}$  and  $U_{nn3}$  are ignored [84] in the second line in Eq. 2.7 normally).

The Eq. 2.7 (the first line) is much simpler than Eq. 2.1. However, it is still not solvable. Further approximations are needed to solve this many-body problem.

### 2.1.3 Hartree, Hartree-Fock approximation and density functional theory

In previous section, the separation of wavefunction is given within Born-Oppenheimer approximation. The quantum many-body Schrödinger problem becomes the many-electron Schrödinger problem. There are two major problems from the Born-Oppenheimer approximation: the first problem is that the number of electron is around in the order of  $10^{24} \text{ cm}^{-3}$  in most of the cases, which is a huge numerical problem. However, it is still possible to solve; the second one is that the Hamiltonian includes operators which apply to the single electron. However, how the wavefunction depends on the single-electron wavefunction is unknown. The latter problem can be solved by one of the following three methods: the first method is to figure out a way to separate or approximate the wavefunction into single-electron function, such as the Hartree and Hartree-Fock (HF) methods [80, 81]; the second method is to find a explicit relation between total energy and wavefunction, such as density functional theory (DFT) [82]. Within DFT, the system total energy is a functional of electron density. Either of these two methods has "pros and cons"; the third one is called Kohn-Sham equation [83], which is a combination of above two methods. It starts from DFT, and takes advantage of single-electron wavefunction.

#### 2.1.3.1 Hartree approximation

The simplest approximation of the wavefunction for the many-electron Schrödinger equation is the one acting like independent electrons. The wavefunction with  $N_e$  independent electrons is defined as

$$\Psi^H(\{\mathbf{r}_i\}) = \phi_1(\mathbf{r}_1)\phi_2(\mathbf{r}_2) \cdots \phi_{N_e}(\mathbf{r}_{N_e}). \quad (2.9)$$

Here,  $i$  goes through the coordinators of all electrons.  $\phi_i(\mathbf{r}_i)$  implies state of the  $i$ :th electron, where the different states of electrons are orthonormalized. From here on, the  $\{\mathbf{R}_I\}$  are suppressed in the wavefunction since they are in fixed positions. The variables  $\{\mathbf{r}_i\}$  include the coordinates of space and spin. The total energy of the electronic system can be written as

$$E^H = \langle \Psi^H(\{\mathbf{r}_i\}) | H | \Psi^H(\{\mathbf{r}_i\}) \rangle . \quad (2.10)$$

$H$  in Eq. 2.4 can be rewritten as

$$\begin{aligned} H &= \sum_i^{Ne} \left( -\frac{\nabla_i^2}{2} - \sum_I^{Nn} \frac{Z_I}{|\mathbf{r}_i - \mathbf{R}_I|} \right) + \frac{1}{2} \sum_i^{Ne} \sum_{j \neq i}^{Ne} \frac{1}{|\mathbf{r}_i - \mathbf{r}_j|} \\ &= \sum_i^{Ne} h_1(\mathbf{r}_i) + \frac{1}{2} \sum_i^{Ne} \sum_{j \neq i}^{Ne} h_2(\mathbf{r}_i, \mathbf{r}_j). \end{aligned} \quad (2.11)$$

Therefore, the system total energy is given as

$$\begin{aligned} E^H &= \sum_i^{Ne} \langle \phi_i(\mathbf{r}_i) | h_1(\mathbf{r}_i) | \phi_i(\mathbf{r}_i) \rangle \\ &\quad + \frac{1}{2} \sum_i^{Ne} \sum_{j \neq i}^{Ne} \langle \phi_i(\mathbf{r}_i) \phi_j(\mathbf{r}_j) | h_2(\mathbf{r}_i, \mathbf{r}_j) | \phi_i(\mathbf{r}_i) \phi_j(\mathbf{r}_j) \rangle . \end{aligned} \quad (2.12)$$

In order to calculate the stationary state with the lowest energy of the system, the method of Lagrange multipliers can be utilized. Furthermore, the constraint is that the different states of electrons are orthonormalized. Therefore, the variation with respect to any wavefunction  $\phi_k^*(\mathbf{r})$  and Lagrange multiplier  $E_{i,j}^H$  is satisfied [84, 85]

$$\frac{\delta \left( E^H - \sum_i^{Ne} \sum_j^{Ne} E_{i,j}^H (\langle \phi_i(\mathbf{r}_i) | \phi_j(\mathbf{r}_j) \rangle - \delta_{ij}) \right)}{\delta \phi_k^*(\mathbf{r})} = 0. \quad (2.13)$$

Here,  $\delta \phi_k(\mathbf{r})$  also can be utilized. However, variation with respect to  $\phi_k^*(\mathbf{r})$  and  $\phi_k(\mathbf{r})$  are equivalent. It is convenient to use  $\delta \phi_k^*(\mathbf{r})$ .

$\delta E^H$  in Eq. 2.13 can be calculated by two parts. The first part is

$$\begin{aligned} &\delta \left( \sum_i^{Ne} \langle \phi_i(\mathbf{r}_i) | h_1(\mathbf{r}_i) | \phi_i(\mathbf{r}_i) \rangle \right) \\ &= \langle \delta \phi_k(\mathbf{r}) | h_1(\mathbf{r}) | \phi_k(\mathbf{r}) \rangle + \langle \phi_k(\mathbf{r}) | h_1(\mathbf{r}) | \delta \phi_k(\mathbf{r}) \rangle . \end{aligned} \quad (2.14)$$

The second part is

$$\begin{aligned}
& \frac{1}{2} \delta \sum_i^{Ne} \sum_{j \neq i}^{Ne} \langle \phi_i(\mathbf{r}_i) \phi_j(\mathbf{r}_j) | h_2(\mathbf{r}_i, \mathbf{r}_j) | \phi_i(\mathbf{r}_i) \phi_j(\mathbf{r}_j) \rangle \\
&= \frac{1}{2} \sum_{i \neq k}^{Ne} \left( \langle \phi_i(\mathbf{r}_i) \delta \phi_k(\mathbf{r}) | h_2(\mathbf{r}_i, \mathbf{r}) | \phi_i(\mathbf{r}_i) \phi_k(\mathbf{r}) \rangle \right. \\
&\quad \left. + \langle \phi_i(\mathbf{r}_i) \phi_k(\mathbf{r}) | h_2(\mathbf{r}_i, \mathbf{r}) | \phi_i(\mathbf{r}_i) \delta \phi_k(\mathbf{r}) \rangle \right) \\
&\quad + \frac{1}{2} \sum_{j \neq k}^{Ne} \left( \langle \delta \phi_k(\mathbf{r}) \delta \phi_j(\mathbf{r}_j) | h_2(\mathbf{r}, \mathbf{r}_j) | \phi_k(\mathbf{r}) \phi_j(\mathbf{r}_j) \rangle \right. \\
&\quad \left. + \langle \phi_k(\mathbf{r}) \phi_j(\mathbf{r}_j) | h_2(\mathbf{r}, \mathbf{r}_j) | \delta \phi_k(\mathbf{r}) \phi_j(\mathbf{r}_j) \rangle \right) \\
&= \sum_{i \neq k}^{Ne} \left( \langle \phi_i(\mathbf{r}_i) \delta \phi_k(\mathbf{r}) | h_2(\mathbf{r}_i, \mathbf{r}) | \phi_i(\mathbf{r}_i) \phi_k(\mathbf{r}) \rangle \right. \\
&\quad \left. + \langle \phi_i(\mathbf{r}_i) \phi_k(\mathbf{r}) | h_2(\mathbf{r}_i, \mathbf{r}) | \phi_i(\mathbf{r}_i) \delta \phi_k(\mathbf{r}) \rangle \right). \tag{2.15}
\end{aligned}$$

Here, the factor of  $\frac{1}{2}$  cancels because the 2nd (3rd) line is the same with 4th (5th) line in Eq. 2.15 due to the exchangeable indices of  $i$  and  $j$ .

To get the final solution, one more calculation is needed

$$\begin{aligned}
& \delta \sum_i^{Ne} \sum_j^{Ne} E_{i,j}^H \left( \langle \phi_i(\mathbf{r}_i) | \phi_j(\mathbf{r}_j) \rangle - \delta_{i,j} \right) \\
&= \sum_j^{Ne} E_{k,j}^H \left( \langle \delta \phi_k(\mathbf{r}) | \phi_j(\mathbf{r}_j) \rangle \right) + \sum_i^{Ne} E_{i,k}^H \left( \langle \phi_i(\mathbf{r}_i) | \delta \phi_k(\mathbf{r}) \rangle \right) \\
&= \sum_i^{Ne} E_{k,i}^H \left( \langle \delta \phi_k(\mathbf{r}) | \phi_i(\mathbf{r}_i) \rangle + \langle \phi_i(\mathbf{r}_i) | \delta \phi_k(\mathbf{r}) \rangle \right). \tag{2.16}
\end{aligned}$$

Therefore, Eq. 2.13 can be derived as

$$\left( -\frac{\nabla_k^2}{2} + \sum_I^{Nn} \frac{Z_I}{|\mathbf{r} - \mathbf{R}_I|} + \sum_{j \neq k}^{Ne} \langle \phi_j(\mathbf{r}') | \frac{1}{|\mathbf{r} - \mathbf{r}'|} | \phi_j(\mathbf{r}') \rangle \right) \phi_k(\mathbf{r}) = \sum_i^{Ne} E_{k,i}^H \phi_i(\mathbf{r}). \tag{2.17}$$

There are many solutions to Eq. 2.17, each corresponding to a different set of  $E_{k,i}^H$ . One can choose to  $E_{k,i}^H$  which satisfies  $E_{k,i}^H = \delta_{k,i} \epsilon_k^H$ . The Eq. 2.17 can be rewritten as

$$\begin{aligned} \left( -\frac{\nabla_k^2}{2} + \sum_I^{Nn} \frac{Z_I}{|\mathbf{r} - \mathbf{R}_I|} + \sum_{j \neq k}^{Ne} \langle \phi_j(\mathbf{r}') | \frac{1}{|\mathbf{r} - \mathbf{r}'|} |\phi_j(\mathbf{r}') \rangle \right) \phi_k(\mathbf{r}) &= \epsilon_k^H \phi_k(\mathbf{r}) \\ &\Downarrow \\ \left( -\frac{\nabla_i^2}{2} + \sum_I^{Nn} \frac{Z_I}{|\mathbf{r} - \mathbf{R}_I|} + \sum_{j \neq i}^{Ne} \langle \phi_j(\mathbf{r}') | \frac{1}{|\mathbf{r} - \mathbf{r}'|} |\phi_j(\mathbf{r}') \rangle \right) \phi_i(\mathbf{r}) &= \epsilon_i^H \phi_i(\mathbf{r}). \end{aligned} \quad (2.18)$$

Here, **Eq. 2.18** is a group of dependent single particle equations.  $\epsilon_k^H$  is identified as the eigenvalue for this single-electron Hartree equation.

### 2.1.3.2 Hartree-Fock approximation

Hartree approximation is a simple approximation, Hartree-Fock approximation is a method which considers the antisymmetry of the wavefunction. It is shown as

$$\Psi^{HF}(\dots \mathbf{r}_i \dots \mathbf{r}_j \dots) = -\Psi^{HF}(\dots \mathbf{r}_j \dots \mathbf{r}_i \dots). \quad (2.19)$$

Here, each variable  $\mathbf{r}_i$  includes the coordinates of space and spin. Slater introduced an way to construct the wavefunction subject to **Eq. 2.19** [86]. The wavefunction of the many-electron Schrödinger equation is described in a matrix determinant for the  $N$  number of electrons (for aesthetic reason,  $N$  implies the number of electrons and not  $Ne$  as in previous sections)

$$\Psi^{HF}(\mathbf{r}_1, \mathbf{r}_2, \dots, \mathbf{r}_N) = \frac{1}{\sqrt{N!}} \begin{vmatrix} \phi_1(\mathbf{r}_1) & \phi_2(\mathbf{r}_1) & \cdots & \phi_N(\mathbf{r}_1) \\ \phi_1(\mathbf{r}_2) & \phi_2(\mathbf{r}_2) & \cdots & \phi_N(\mathbf{r}_2) \\ \vdots & \vdots & & \vdots \\ \phi_1(\mathbf{r}_N) & \phi_2(\mathbf{r}_N) & \cdots & \phi_N(\mathbf{r}_N) \end{vmatrix}. \quad (2.20)$$

Here, the factor in front ensures normalization,  $i$  goes through all the electrons, and  $\phi_i(\mathbf{r}_i)$  implies state of the ( $i$ ):th electron. If two rows in **Eq. 2.20** are exchanged, the result is in agreement with **Eq. 2.19**.

The total energy of Hartree-Fock approximation, which can be determined similarly as in the previous section of Hartree approximation, is given as

$$\begin{aligned} E^{HF} &= \sum_i^N \langle \phi_i(\mathbf{r}) | -\frac{\nabla_i^2}{2} + \sum_I^{Nn} \frac{Z_I}{|\mathbf{r} - \mathbf{R}_I|} |\phi_i(\mathbf{r}) \rangle \\ &+ \frac{1}{2} \sum_i^N \sum_j^N \langle \phi_i(\mathbf{r}) \phi_j(\mathbf{r}') | \frac{1}{|\mathbf{r} - \mathbf{r}'|} |\phi_i(\mathbf{r}) \phi_j(\mathbf{r}') \rangle \\ &- \frac{1}{2} \sum_i^N \sum_j^N \langle \phi_i(\mathbf{r}') \phi_j(\mathbf{r}) | \frac{1}{|\mathbf{r} - \mathbf{r}'|} |\phi_i(\mathbf{r}) \phi_j(\mathbf{r}') \rangle. \end{aligned} \quad (2.21)$$

Here, there is no contribution to the sum when  $i = j$ . In the same mathematical way as in previous section but somewhat more complicated, the single particle Hartree-Fock equation can be obtained

$$\begin{aligned} & \left( -\frac{\nabla_i^2}{2} + \sum_I^{Nn} \frac{Z_I}{|\mathbf{r} - \mathbf{R}_I|} + \sum_j^N \langle \phi_j(\mathbf{r}') | \frac{1}{|\mathbf{r} - \mathbf{r}'|} |\phi_j(\mathbf{r}') \rangle \right) \phi_i(\mathbf{r}) \\ & - \sum_j^N \langle \phi_j(\mathbf{r}') | \frac{1}{|\mathbf{r} - \mathbf{r}'|} |\phi_i(\mathbf{r}') \rangle \phi_j(\mathbf{r}) = \epsilon_i^{HF} \phi_i(\mathbf{r}). \end{aligned} \quad (2.22)$$

In comparison with Hartree equation in Eq. 2.18, there is an extra term in Eq. 2.22, which is so called exchange term. In order to show the equation in a more well organized way, Eq. 2.22 is equivalent to

$$\begin{aligned} & \left( -\frac{\nabla_i^2}{2} + \sum_I^{Nn} \frac{Z_I}{|\mathbf{r} - \mathbf{R}_I|} + V_{HF}(\mathbf{r}) \right) \phi_i(\mathbf{r}) = \epsilon_i^{HF} \phi_i(\mathbf{r}) \\ & V_{HF}(\mathbf{r}) = \int \frac{\rho(\mathbf{r}') - \rho_i^{HF}(\mathbf{r}, \mathbf{r}')}{|\mathbf{r} - \mathbf{r}'|} d\mathbf{r}' \\ & \rho_i^{HF}(\mathbf{r}, \mathbf{r}') = \sum_j^N \frac{\phi_i(\mathbf{r}') \phi_i^*(\mathbf{r}) \phi_j(\mathbf{r}) \phi_j^*(\mathbf{r}')}{\phi_i(\mathbf{r}) \phi_i^*(\mathbf{r})} \\ & \rho(\mathbf{r}) = \sum_i^N |\phi_i(\mathbf{r})|^2. \end{aligned} \quad (2.23)$$

### 2.1.3.3 Density functional theory

The Hartree and HF methods are very classic methods to solve the many-electron Schrödinger equation. However, the HF method only includes the exchange term and not the electron correlation term. Therefore, it is not suitable for the solid materials. Apart from the Hartree and HF methods, there is a modern method to solve the more complicated calculations of electronic system, namely density functional theory (DFT). It is introduced by Hohenberg and Kohn in 1964 [82], Kohn and Pople was awarded Chemistry Nobel Prize in 1998.

The idea of the DFT is to treat the electron density in solid materials instead of using the many-particle wavefunction. One can benefit that the degree of freedom reduces from  $3N$  ( $N$  is the number of electrons) to 3. It is apparently less complicate than those of Hartree and HF methods.

#### The density as basic variable

There are two questions coming out if considering the electron density as the role of wavefunction. The first one is whether it is the equivalence relation between the elec-

tron density and wavefunction in the electron system. The second one is how to solve the problem if considering the electron density instead of the wavefunction. In order to explain above two questions, there are two very basic theorems introduced by Hohenberg and Kohn:

**Theorem 1** *The first theorem states that the external potential  $V_{ext}(\mathbf{r})$  is determined uniquely for any electron system by the ground-state electron density  $\rho$ .*

The above theorem indicates that all the ground state properties are determined by the true ground-state density  $\rho$  as well, such as, the total energy  $E = E[\rho]$ .

The above theorem also explains the equivalence relation between the electron density and wavefunction. Because Hamiltonian is obtained from external potential, then the wavefunction is obtained. Therefore the corresponding electron density is determined. Moreover, from the theorem, the external potential is unique decided by electron density. Therefore the electron density contains the same information as the wavefunction.

The proof of the theorem is given. Let us assume that there exists two external potentials named  $V_{ext}(\mathbf{r})$  and  $V'_{ext}(\mathbf{r})$  leading to the same ground state electron density  $\rho$ . Obviously, this will lead to two different Hamiltonians, that is,  $H$  and  $H'$ , as well as two different corresponding wavefunctions named  $\Psi$  and  $\Psi'$ . Since  $\Psi$  are not the ground state wavefunction of  $H'$ , the same rules to  $\Psi'$  and  $H$ , two following inequality equations are satisfied

$$\begin{aligned} E &= \langle \Psi | H | \Psi \rangle < \langle \Psi' | H | \Psi' \rangle \\ E' &= \langle \Psi' | H' | \Psi' \rangle < \langle \Psi | H' | \Psi \rangle. \end{aligned} \quad (2.24)$$

Taking advantage of the Hamiltonian from **Eq. 2.4**, the following equation is derived

$$\begin{aligned} &\langle \Psi' | H | \Psi' \rangle \\ &= \langle \Psi' | H' + H - H' | \Psi' \rangle \\ &= \langle \Psi' | H' | \Psi' \rangle + \langle \Psi' | H - H' | \Psi' \rangle \\ &= E' + \int \left( V_{ext}(\mathbf{r}) - V'_{ext}(\mathbf{r}) \right) \rho(\mathbf{r}) d\mathbf{r}. \end{aligned} \quad (2.25)$$

Using **Eq. 2.24** and **Eq. 2.25**, the following relation is given by

$$E < E' + \int \left( V_{ext}(\mathbf{r}) - V'_{ext}(\mathbf{r}) \right) \rho(\mathbf{r}) d\mathbf{r}. \quad (2.26)$$

Another similar inequality equation can be gained if one changes the equation  $\langle \Psi | H' | \Psi \rangle$  like **Eq. 2.25**

$$E' < E + \int \left( V'_{ext}(\mathbf{r}) - V_{ext}(\mathbf{r}) \right) \rho(\mathbf{r}) d\mathbf{r}. \quad (2.27)$$

Plus the left side and right side from both Eq. 2.26 and eq. 2.27, a contradictory result is given as

$$E + E' < E' + E. \quad (2.28)$$

Since this is an incorrect relation, the external potential  $V_{ext}(\mathbf{r})$  has to be unique.

**Theorem 2** *The second theorem states that there is a universal functional  $F[\rho]$  for the total energy in the terms of the electron density  $\rho$  with any external potential  $V_{ext}(\mathbf{r})$ , and the exact ground-state density is gained when the ground state total energy functional reaches its minimal value, that is,  $E[\rho'] > E[\rho]$ . Here,  $\rho$  is the exact ground-state density.*

The proof of theorem is given. Because of the first theorem, the kinetic and interaction energy are functional of electron density. The total energy can be expressed in the following way (ignoring the interaction between nuclei)

$$\begin{aligned} E[\rho] &= \langle \Psi | U_e + U_{int} + U_{ext} | \Psi \rangle \\ &= \langle \Psi | V_{ext}(\mathbf{r}) | \Psi \rangle + \underbrace{\langle \Psi | U_e + U_{int} | \Psi \rangle}_{\text{}} \\ &= \int \rho(\mathbf{r}) V_{ext}(\mathbf{r}) d\mathbf{r} + F[\rho]. \end{aligned} \quad (2.29)$$

In Eq. 2.29, the term of  $F[\rho]$  is the universal functional for all the many-electron system. The functional of total energy  $E[\rho']$  reach the minimum at the exact ground-state electron density  $\rho$

$$E[\rho'] = \int \rho'(\mathbf{r}) V_{ext}(\mathbf{r}) d\mathbf{r} + F[\rho'] > E[\rho]. \quad (2.30)$$

Here, the total energy for the case of exact ground-state electron density is lower than any other cases. Therefore, the exact ground-state electron density by minimizing the total energy can be achieved.

From those two theorems, one knows how to solve Schrödinger equation theoretically. However,  $E[\rho]$  is unknown in practice. Therefore, another method is needed to solve it, which is so called Kohn-Sham (KS) equation.

#### 2.1.3.4 Kohn-Sham equation

The Hartree and Hartree-Fock methods are introduced to solve the many-body problem, both of which are based on the idea of transforming complex many-electron problem to single-electron problem by using different wavefunctions. The DFT gives the answer to solve many-electron system, however, it does not give explicit expression. The problem in DFT is solved by Kohn-Sham equation that is introduced by Kohn and Sham in 1965 [83]. It is demonstrated in the following text (ignoring the interaction between nuclei).

Assume that the exact ground-state density is obtained by the Hartree-like wavefunction  $\Psi^{KS}(\{\mathbf{r}_i\}) = \Psi_1^{KS}(\mathbf{r}_1)\Psi_2^{KS}(\mathbf{r}_2)\dots\Psi_N^{KS}(\mathbf{r}_N)$ . Here,  $N$  is a number of electrons and  $\Psi_i^{KS}(\mathbf{r}_i)$  is auxiliary independent single-electron wavefunctions. The electron density is defined as

$$\rho(\mathbf{r}) = \sum_i^N \Psi_i^{KS*}(\mathbf{r})\Psi_i^{KS}(\mathbf{r}). \quad (2.31)$$

If the electron density is exact, the total energy is exact. It is given as

$$\begin{aligned} E[\rho] &= T[\rho] + V_{int}[\rho] + V_{ext}[\rho] \\ &= T_0[\rho] + V_H[\rho] + V_{ext}[\rho] + \underbrace{(T[\rho] - T_0[\rho])}_{(V_{int}[\rho] - V_H[\rho])} \\ &= T_0[\rho] + V_H[\rho] + V_{ext}[\rho] + E_{xc}[\rho]. \end{aligned} \quad (2.32)$$

Here,  $E[\rho]$  is the total energy, and  $\rho$  is the ground-state density.  $T[\rho]$ ,  $V_{int}[\rho]$ , and  $V_{ext}[\rho]$  are the energy from the exact kinetic, the exact electron-electron potential, and external potential in sequence.  $E_{xc}[\rho]$  is unknown exchange-correlation energy.

The  $T_0[\rho]$ ,  $V_H[\rho]$ , and  $V_{ext}[\rho]$  are kinetic energy in the Hartree approximation, electron interaction energy in Hartree approximation, and electron-nuclei interaction energy in sequence.

$$\begin{aligned} T_0[\rho] &= \sum_i^N \langle \Psi_i^{KS}(\mathbf{r}) | -\frac{\nabla^2}{2} | \Psi_i^{KS}(\mathbf{r}) \rangle \\ V_H[\rho] &= \frac{1}{2} \int \int \frac{\rho(\mathbf{r})\rho(\mathbf{r}')}{|\mathbf{r} - \mathbf{r}'|} d\mathbf{r}d\mathbf{r}' \\ V_{ext}[\rho] &= \int \rho(\mathbf{r})V_{ext}(\mathbf{r})d\mathbf{r}. \end{aligned} \quad (2.33)$$

In order to derive the ground state properties in the many-electron system, one can view this problem as the process of minimizing the total energy by varying the wavefunction  $\Psi_k^{KS*}(\mathbf{r})$ .

$$\begin{aligned} \frac{\delta \left( E[\rho] - \sum_i^{Ne} \sum_j^{Ne} E_{i,j}^H (\langle \Psi_i^{KS}(\mathbf{r}_i) | \Psi_j^{KS}(\mathbf{r}_j) \rangle - \delta_{ij}) \right)}{\delta \Psi_i^{KS*}(\mathbf{r})} &= 0 \\ \downarrow \\ \frac{\delta T_0[\rho]}{\Psi_k^{KS*}(\mathbf{r})} + \frac{\delta(V_H[\rho] + V_{ext}[\rho] + E_{xc}[\rho])}{\delta \rho(\mathbf{r})} \frac{\delta \rho(\mathbf{r})}{\Psi_i^{KS*}(\mathbf{r})} &= \sum_i^N E_{k,i}^{KS} \Psi_i^{KS}(\mathbf{r}). \end{aligned} \quad (2.34)$$

The derivation is similar as in the section of Hartree approximation, the Kohn-Sham equation is derived as

$$\left( -\frac{\nabla^2}{2} + V^{KS}(\mathbf{r}) \right) \Psi_i^{KS}(\mathbf{r}) = \epsilon_i^{KS} \Psi_i^{KS}(\mathbf{r}). \quad (2.35)$$

Here,  $\epsilon_i^{KS}$  is identified as eigenvalue for the Kohn-Sham equation. The  $V^{KS}(\mathbf{r})$  is

$$\begin{aligned} V^{KS}(\mathbf{r}) &= V_{ext}(\mathbf{r}) + \int d\mathbf{r}' \frac{\rho(\mathbf{r}')}{|\mathbf{r} - \mathbf{r}'|} + \frac{\delta E_{xc}}{\delta \rho(\mathbf{r})} \\ &= V_{ext}(\mathbf{r}) + \int d\mathbf{r}' \frac{\rho(\mathbf{r}')}{|\mathbf{r} - \mathbf{r}'|} + V_{xc}(\mathbf{r}). \end{aligned} \quad (2.36)$$

In  $\mathbf{k}$ -space, Kohn-Sham equation in Eq. 2.35 can be written as

$$\left( -\frac{\nabla^2}{2} + V^{KS}(\mathbf{r}) \right) \Psi_{i,k}^{KS}(\mathbf{r}) = \epsilon_{i,k}^{KS} \Psi_{i,k}^{KS}(\mathbf{r}). \quad (2.37)$$

The total energy is not given in Eq. 2.35. However, if one changes Eq. 2.35 as

$$\sum_i^N \Psi_i^{KS*}(\mathbf{r}) \left( -\frac{\nabla^2}{2} + V^{KS}(\mathbf{r}) \right) \Psi_i^{KS}(\mathbf{r}) = \sum_i^N \Psi_i^{KS*}(\mathbf{r}) \epsilon_i^{KS} \Psi_i^{KS}(\mathbf{r}). \quad (2.38)$$

Based on Eq. 2.33 , Eq. 2.32 and Eq. 2.38, the total energy expression is derived as

$$\begin{aligned} E[\rho] &= \sum_i^N \epsilon_i^{KS} - \frac{1}{2} \int \int d\mathbf{r} d\mathbf{r}' \frac{\rho(\mathbf{r}) \rho(\mathbf{r}')}{|\mathbf{r} - \mathbf{r}'|} \\ &\quad + E_{xc}[\rho] - \int V_{xc}(\mathbf{r}) \rho(\mathbf{r}) d\mathbf{r}. \end{aligned} \quad (2.39)$$

There are two problems still in the air: one is the exact format of  $V_{xc}(\mathbf{r})$ ; the other one is how to solve the Kohn-Sham equation.

### 2.1.3.5 The exchange-correlation potential

The exchange-correlation potential is the most difficult part during the process of solving the Kohn-Sham equation, because it is still unknown today. Therefore, there are varies of approximations about it, such as the local density approximation (LDA) [77, 78, 83, 87, 88].

#### The local density approximation

The local density approximation is the simplest way to approximate the exchange-correlation part. It is based on free electron gas which has a constant electron density

$$\rho(\mathbf{r}) = \rho = \frac{N}{V}. \quad (2.40)$$

Here,  $N$  is number of electrons within the solid, and  $V$  is the volume of solid. The exact exchange-correlation energy per electron is given as

$$\varepsilon_{xc}^{gas}(\rho) = -\frac{3}{4} \cdot \left(\frac{3}{\pi}\right)^{1/3} \cdot \rho^{1/3} + \begin{cases} A \ln r_s + B + C r_s \ln r_s + D r_s & \text{if } r_s \leq 1 \\ \gamma / (1 + \beta_1 \sqrt{r_s} + \beta_2 r_s) & \text{if } r_s > 1. \end{cases} \quad (2.41)$$

Here,  $r_s = (3/(4\pi\rho))^{1/3}$ . In the LDA, the idea is that the exchange-correlation energy for an electron in the very tiny small volume in many-particle system is equal to the exchange-correlation for an electron in the free electron gas with the same density in the volume ( $\varepsilon_{xc}^{gas}(\rho(\mathbf{r})) = \varepsilon_{xc}^{gas}(\mathbf{r})$ ). The explicit exchange-correlation energy is given as

$$E_{xc}^{LDA}[\rho] = \int \rho(\mathbf{r}) \varepsilon_{xc}^{gas}(\mathbf{r}) d\mathbf{r}. \quad (2.42)$$

Therefore, the exchange-correlation potential is give as

$$V_{xc}^{LDA}(\mathbf{r}) = \frac{\delta E_{xc}^{LDA}[\rho]}{\delta \rho}. \quad (2.43)$$

Today, there exists hundreds of different exchange-correlation potentials [89–92]. It is still ongoing development. The advantage of Kohn-Sham equation is that new potentials are implemented easily. In the same time, the number of potential is huge due to the simplicity of implementation.

#### 2.1.4 Solving the secular equation

The process for solving Kohn-Sham equation can be achieved by iteration [77, 78, 84]. Because potentials in Kohn-Sham equation depends on electron density. However, electron density is calculated by wavefunction which depends on potential. An initial guess of electron density is calculated at the beginning of the calculation, then the equation is solved iteratively until the reasonable solution is obtained.

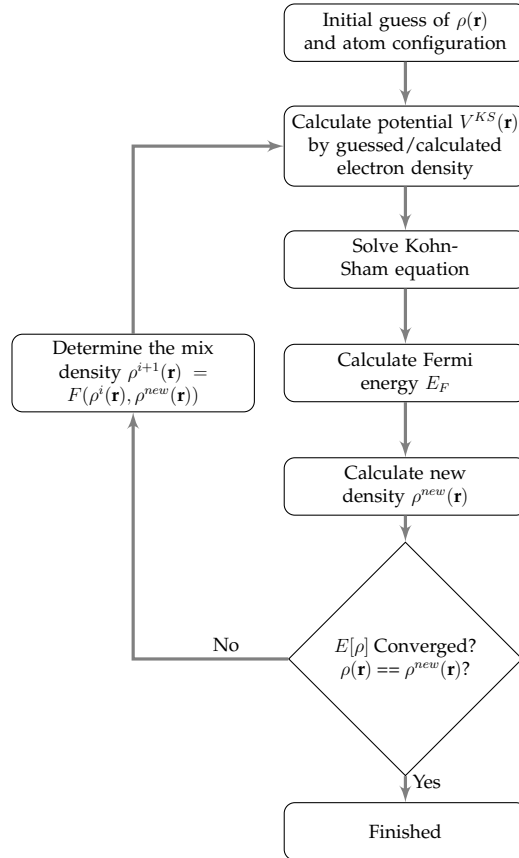


**Figure 2.1.** Flow chart of the  $(i + 1)$ :th iteration for solving Kohn-Sham equation.

Here,  $\rho^i(\mathbf{r})$  and  $\rho^{i+1}(\mathbf{r})$  are the electron density in the  $i$ :th iteration and  $(i + 1)$ :th iteration during solving Kohn-Sham equation, respectively.

### 2.1.5 Eigenvalue problem

In order to solve [Eq. 2.35](#), the Kohn-Sham equation can be transformed into the general eigenvalue problem [77, 78]. If the Kohn-Sham equation is given as (ignore the index  $i$  in wavefunction compared with [Eq. 2.35](#))

$$H^{KS}\Psi^{KS}(\mathbf{r}) = \epsilon^{KS}\Psi^{KS}(\mathbf{r}). \quad (2.44)$$

The wavefunction is defined as

$$\Psi^{KS}(\mathbf{r}) = \sum_j^N C_j \phi_j(\mathbf{r}). \quad (2.45)$$

Here,  $C_j$  is a complex number, and  $\phi_j(\mathbf{r})$  is the basis function of wavefunction.

If [Eq. 2.45](#) is plugged into [Eq. 2.44](#), and left multiply  $\phi_1^*, \phi_2^*, \dots, \phi_N^*$  in sequence, it ends up with a set of equations

$$\begin{aligned} & \begin{bmatrix} \phi_1^* H \phi_1 & \phi_1^* H \phi_2 & \cdots & \phi_1^* H \phi_N \\ \phi_2^* H \phi_1 & \phi_2^* H \phi_2 & \cdots & \phi_2^* H \phi_N \\ \vdots & \vdots & & \vdots \\ \phi_N^* H \phi_1 & \phi_N^* H \phi_2 & \cdots & \phi_N^* H \phi_N \end{bmatrix} \begin{bmatrix} C_1 \\ C_2 \\ \vdots \\ C_N \end{bmatrix} \\ &= \epsilon^{KS} \begin{bmatrix} \phi_1^* \phi_1 & \phi_1^* \phi_2 & \cdots & \phi_1^* \phi_N \\ \phi_2^* \phi_1 & \phi_2^* \phi_2 & \cdots & \phi_2^* \phi_N \\ \vdots & \vdots & & \vdots \\ \phi_N^* \phi_1 & \phi_N^* \phi_2 & \cdots & \phi_N^* \phi_N \end{bmatrix} \begin{bmatrix} C_1 \\ C_2 \\ \vdots \\ C_N \end{bmatrix}. \end{aligned} \quad (2.46)$$

One defines that  $H_{ij} = \phi_i^* H \phi_j$  and  $S_{ij} = \phi_i^* \phi_j$ . Therefore, [Eq. 2.46](#) becomes

$$\begin{aligned} & \begin{bmatrix} H_{11} & H_{12} & \cdots & H_{1N} \\ H_{21} & H_{22} & \cdots & H_{2N} \\ \vdots & \vdots & & \vdots \\ H_{N1} & H_{N2} & \cdots & H_{NN} \end{bmatrix} \begin{bmatrix} C_1 \\ C_2 \\ \vdots \\ C_N \end{bmatrix} \\ &= \epsilon^{KS} \begin{bmatrix} S_{11} & S_{12} & \cdots & S_{1N} \\ S_{21} & S_{22} & \cdots & S_{2N} \\ \vdots & \vdots & & \vdots \\ S_{N1} & S_{N2} & \cdots & S_{NN} \end{bmatrix} \begin{bmatrix} C_1 \\ C_2 \\ \vdots \\ C_N \end{bmatrix}. \end{aligned} \quad (2.47)$$

There are left part and right part in [Eq. 2.47](#). If the right part moves to the left part, and do the subtraction. The new equation is given as

$$\begin{bmatrix} H_{11} - \epsilon^{KS} S_{11} & H_{12} - \epsilon^{KS} S_{12} & \cdots & H_{1N} - \epsilon^{KS} S_{1N} \\ H_{21} - \epsilon^{KS} S_{21} & H_{22} - \epsilon^{KS} S_{22} & \cdots & H_{2N} - \epsilon^{KS} S_{2N} \\ \vdots & \vdots & & \vdots \\ H_{N1} - \epsilon^{KS} S_{N1} & H_{N2} - \epsilon^{KS} S_{N2} & \cdots & H_{NN} - \epsilon^{KS} S_{NN} \end{bmatrix} \begin{bmatrix} C_1 \\ C_2 \\ \vdots \\ C_N \end{bmatrix} = \begin{bmatrix} 0 \\ 0 \\ \vdots \\ 0 \end{bmatrix}. \quad (2.48)$$

Apparently, **Eq. 2.48** is an eigenvalue problem. In order to get the  $C_i (i = 1 \dots N)$ , one needs to solve the eigenvalue problem

$$\begin{vmatrix} H_{11} - \epsilon^{KS} S_{11} & H_{12} - \epsilon^{KS} S_{12} & \cdots & H_{1N} - \epsilon^{KS} S_{1N} \\ H_{21} - \epsilon^{KS} S_{21} & H_{22} - \epsilon^{KS} S_{22} & \cdots & H_{2N} - \epsilon^{KS} S_{2N} \\ \vdots & \vdots & & \vdots \\ H_{N1} - \epsilon^{KS} S_{N1} & H_{N2} - \epsilon^{KS} S_{N2} & \cdots & H_{NN} - \epsilon^{KS} S_{NN} \end{vmatrix} = 0. \quad (2.49)$$

## 2.2 Full-potential linearized augmented plane wave method

### 2.2.1 Introduction

One knows how to solve the Kohn-Sham equation from previous sections. However, there are still two more questions, what is the exact form of wavefunction and potential in the realistic calculations?

One maybe naturally choose a set of plane waves as the wavefunction because of Bloch theory [93]. There is a drawback about the plane waves as wavefunction when describing the atomic core region. Because the wavefunction change dramatically in that region, therefore one needs to choose relatively more plane waves to approximate it. It implies that it takes more time to calculate.

Slater re-considered the way to describe the wavefunction (**Eq. 2.51**). The unit cell is divided into two regions [94, 95]: one is the sphere region which is defined by the center of atom, but non-overlap each sphere, is called muffin tin (MT) region; the remaining region is called interstitial (*I*) region (**Fig. 2.2**). An atomic-like function is defined as the wavefunction in the MT region, this is reason why this method is called augmented plane wave (APW). The dual representation of the wavefunction is reasonable, because the wavefunction approaching atomic core is somehow like inside atom. However, the electron behaves like free electrons far away the atomic core. Therefore plane waves are suitable (**Eq. 2.51**). The drawback of APW method is that the wavefunction is dependent with the energy, which leads to the nonlinear eigenvalue problem (**Eq. 2.52**). This method has to decide repeatedly until certain condition is satisfied to achieve the exact energy, which is really time-consuming.

In order to find a way out, Andesen [96], Koelling and Arbman [97] proposed a way to describe the wavefunction energy-independent. They noticed that the Taylor expansion of radial function (Eq. 2.55). This method is called linearized augmented plane wave (LAPW) method due to make use of the linearized energies in the radial functions. However, the drawback is that it does not describe the semicore state well. It is corrected by a method named linearized augmented plane wave plus local orbitals (LAPW+LO) which is proposed by Singh (Eq. 2.57) [98]. Sjöstedt, Nordström and Singh [99] also give an efficient way to linearize Slater's APW method, named augmented plane wave plus local orbitals (APW+lo) (Eq. 2.58). Both of above methods consider local orbitals, it is customary to write in different ways as LO and lo, respectively. One can read more information about FPLAPW method from Refs [100, 101].

## 2.2.2 Wavefunction

### 2.2.2.1 Augmented plane wave method

The Kohn-Sham wavefunction can be expanded by a set of basis functions

$$\Psi_{i,\mathbf{k}}^{KS}(\mathbf{r}) = \sum_{\mathbf{G}}^{N_G} C_{i,\mathbf{k}+\mathbf{G}} \phi_{\mathbf{k}+\mathbf{G}}(\mathbf{r}). \quad (2.50)$$

Here,  $\phi_{\mathbf{k}+\mathbf{G}}(\mathbf{r})$  is the basis function of wavefunction. It is written in slightly different format in order to distinct the different methods in the following text, for example,  $\phi_{\mathbf{k}+\mathbf{G}}^{APW}(\mathbf{r})$  represents the basis function for the augmented plane wave (APW) method.

The basis set for APW is defined by Slater

$$\phi_{\mathbf{k}+\mathbf{G}}^{APW}(\mathbf{r}) = \begin{cases} \frac{1}{\sqrt{\Omega}} e^{i(\mathbf{k}+\mathbf{G})\mathbf{r}} & \text{if } \mathbf{r} \in I \\ \sum_{\alpha}^{N_{\alpha}} \sum_{\ell}^{N_{\ell}} \sum_{m}^{N_m} f_{\ell m}(r_{\alpha}, \mathbf{k} + \mathbf{G}) Y_{\ell m}(\hat{\mathbf{r}}_{\alpha}) & \text{if } r_{\alpha} \in MT. \end{cases} \quad (2.51)$$

Here,  $f_{\ell m}(r_{\alpha}, \mathbf{k} + \mathbf{G}) = A_{\ell m}^{\alpha}(\mathbf{k} + \mathbf{G}) u_{\ell}(r_{\alpha})$ , and  $A_{\ell m}^{\alpha}(\mathbf{k} + \mathbf{G})$  is the expansion coefficients. The radial function can be decided by Eq. 2.52, where the radial function  $u_{\ell}(r_{\alpha})$  is dependent with energy  $\epsilon_{i,k}^{KS}$ .

$$-\frac{1}{r^2} \frac{d}{dr} (r^2 \frac{du_{\ell}}{dr}) + \left( \frac{\ell(\ell+1)}{r^2} + V_0^{KS}(r) \right) u_{\ell}(r_{\alpha}) = \epsilon_{i,k}^{KS} u_{\ell}(r_{\alpha}). \quad (2.52)$$

In MT region,  $V^{KS}(\mathbf{r})$  is assumed to be spherically symmetric, and it can be substituted by its spherical average  $V_0^{KS}(r)$ .

Because the wavefunction has dual representation, one has to make sure the continuity on the sphere boundary, which is solved by matching each  $\ell m$  of the dual representation.

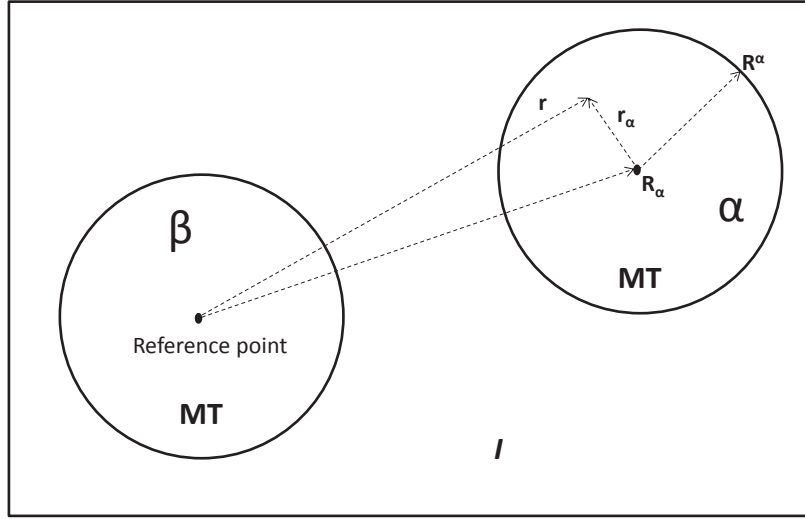


**Figure 2.2.** Partition of the unit cell.

From **Fig. 2.2**, one notices that unit cell is divided into MT spheres ( $\alpha, \beta$ ) and an ( $I$ ) region, where  $\mathbf{r} = \mathbf{R}_\alpha + \mathbf{r}_\alpha$  is guaranteed. The Rayleigh expansion formula yields

$$e^{i(\mathbf{k}+\mathbf{G})\mathbf{r}} = e^{i(\mathbf{k}+\mathbf{G})\mathbf{R}_\alpha} 4\pi \sum_{\ell}^{N_\ell} \sum_m^{N_m} i^\ell j_\ell(|\mathbf{k} + \mathbf{G}|r_\alpha) Y_{\ell m}(\hat{\mathbf{r}}_\alpha) \widehat{Y_{\ell m}(\mathbf{k} + \mathbf{G})}. \quad (2.53)$$

After matching those two representations, the following equation is satisfied for each  $\ell m$

$$A_{\ell m}^\alpha(\mathbf{k} + \mathbf{G}) u_\ell^\alpha(r_\alpha) = \frac{4\pi}{\sqrt{\Omega}} e^{i(\mathbf{k}+\mathbf{G})\mathbf{R}_\alpha} \sum_{\ell}^{N_\ell} \sum_m^{N_m} i^\ell j_\ell(|\mathbf{k} + \mathbf{G}|r_\alpha) Y_{\ell m}^*(\widehat{\mathbf{k} + \mathbf{G}}). \quad (2.54)$$

The main drawbacks about the APW method is that the wavefunction is energy dependent (Eq. 2.52). The calculation needs to search for the energy in order to calculate the exact energy. Therefore it is really time-consuming.

### 2.2.2.2 Linearized augmented plane wave method

In order to decouple the energy from the wavefunction, Andesen, Koelling and Arbman found out a way to separate them. They noticed that the Taylor expansion of the radial function on certain energy, which can be given as

$$u_\ell(r_\alpha, \epsilon) = u_\ell(r_\alpha, \epsilon_{\ell,\alpha}) + (\epsilon - \epsilon_{\ell,\alpha}) \dot{u}_\ell(r_\alpha, \epsilon_{\ell,\alpha}) + O((\epsilon - \epsilon_{\ell,\alpha})^2). \quad (2.55)$$

Here, eigenvalue is written without subscript and superscript  $\epsilon$ . Thus, the basis function is re-defined as

$$\phi_{\mathbf{k}+\mathbf{G}}^{LAPW}(\mathbf{r}) = \begin{cases} \frac{1}{\sqrt{\Omega}} e^{i(\mathbf{k}+\mathbf{G})\mathbf{r}} & \text{if } \mathbf{r} \in I \\ \sum_{\alpha} \sum_{\ell m} f_{\ell m}(r_{\alpha}, \mathbf{k} + \mathbf{G}, \epsilon_{\ell, \alpha}) Y_{\ell m}(\hat{\mathbf{r}}_{\alpha}) & \text{if } r_{\alpha} \in MT. \end{cases} \quad (2.56)$$

Here,  $f_{\ell m}(r_{\alpha}, \mathbf{k} + \mathbf{G}, \epsilon_{\ell, \alpha}) = A_{\ell m}^{\alpha}(\mathbf{k} + \mathbf{G}) u_{\ell}(r_{\alpha}, \epsilon_{\ell, \alpha}) + B_{\ell m}^{\alpha}(\mathbf{k} + \mathbf{G}) \dot{u}_{\ell}(r_{\alpha}, \epsilon_{\ell, \alpha})$ .  $A_{\ell m}^{\alpha}(\mathbf{k} + \mathbf{G})$  and  $B_{\ell m}^{\alpha}(\mathbf{k} + \mathbf{G})$  are the expansion coefficients, and  $\dot{u}_{\ell}(r_{\alpha}, \epsilon_{\ell, \alpha})$  is the derivative of the radial function. Energy  $\epsilon_{\ell, \alpha}$  is considered as pre-calculated parameter in Eq. 2.56. Actually, it is chosen by the middle of each  $\ell$ -character band. Therefore this method is called linearized augmented plane wave (LAPW) method.

Apparently, LAPW method is more suitable in reality, because the wavefunction is decoupled with energy. However it has to match for two parameters. Fortunately, it still take less time comparing with APW method. However, there is one drawback about this method, what if energy in the same  $\ell$ -character is different enough, which  $\epsilon_{\ell, \alpha}$  is correct? These states are called as semi-core states which exist in the actinides and the rare earths.

### 2.2.2.3 Linearized augmented plane wave method plus local orbitals

Comparing with LAPW method, a small number of basis set is added in linearized augmented plane wave method plus local orbitals (LAPW+LO) method, which is defined as

$$\phi_{\mathbf{k}+\mathbf{G}}^{LO}(\mathbf{r}) = \begin{cases} 0 & \text{if } \mathbf{r} \in I \\ (A_{\ell m}^{\alpha, LO} u_{\ell}(r_{\alpha}, \epsilon_{\ell, \alpha}) + B_{\ell m}^{\alpha, LO} \dot{u}_{\ell}(r_{\alpha}, \epsilon_{\ell, \alpha}) + C_{\ell m}^{\alpha, LO} u_{\ell}(r_{\alpha}, \epsilon'_{\ell, \alpha})) Y_{\ell m}(\hat{\mathbf{r}}_{\alpha}) & \text{if } r_{\alpha} \in MT. \end{cases} \quad (2.57)$$

Here,  $A_{\ell m}^{\alpha, LO}$ ,  $B_{\ell m}^{\alpha, LO}$ , and  $C_{\ell m}^{\alpha, LO}$  can be obtained by normalization, as well as value and derivation on the sphere boundary to zero. The  $\epsilon'_{\ell, \alpha}$  is the chosen energy from semi-core state.

### 2.2.2.4 Augmented plane wave method plus local orbitals

There is one method which can solve the APW method efficiently, which is called as augmented plane wave method plus local orbitals (APW+lo). The basis function has two types: one is similar with APW method, but only without the derivative terms, that is,  $f_{\ell m}(r_{\alpha}, \mathbf{k} + \mathbf{G}, \epsilon_{\ell, \alpha}) = A_{\ell m}^{\alpha}(\mathbf{k} + \mathbf{G}) u_{\ell}(r_{\alpha}, \epsilon_{\ell, \alpha})$ ; the other basis function is

$$\phi_{\mathbf{k}+\mathbf{G}}^{lo}(\mathbf{r}) = \begin{cases} 0 & \text{if } \mathbf{r} \in I \\ (A_{\ell m}^{\alpha, lo} u_{\ell}(r_{\alpha}, \epsilon_{\ell, \alpha}) + B_{\ell m}^{\alpha, lo} \dot{u}_{\ell}(r_{\alpha}, \epsilon_{\ell, \alpha})) Y_{\ell m}(\hat{\mathbf{r}}_{\alpha}) & \text{if } r_{\alpha} \in MT. \end{cases} \quad (2.58)$$

The value of  $A_{\ell m}^{\alpha,lo}$  and  $B_{\ell m}^{\alpha,lo}$  are obtained by normalization and local orbital has zero value at the muffin tin boundary. This method is not suitable for the calculations considering semicore states. However, it does increase the efficiency. Certainly, it exists some types of basis function which can mix the advantages from mentioned methods.

### 2.2.3 Effective potential

The potential in the FPLAPW method is also divided into two regions, the MT region and the  $I$  region [100].

$$V(\mathbf{r}) = \begin{cases} \sum_{\mathbf{G}} V_{\mathbf{G}} e^{i\mathbf{Gr}} & \text{if } \mathbf{r} \in I \\ \sum_{\ell m} V_{\ell m}^{\alpha}(r_{\alpha}) Y_{\ell m}(\hat{\mathbf{r}}_{\alpha}) & \text{if } r_{\alpha} \in MT. \end{cases}$$

## 2.3 Dielectric function

The dielectric function describes the optical property of materials [102, 103]. Normally, it is written as  $\varepsilon(\omega)$ , which has two parts

$$\varepsilon(\omega) = \varepsilon_1(\omega) + i\varepsilon_2(\omega). \quad (2.59)$$

Here,  $\varepsilon_1(\omega)$  denotes how much the material is polarized when an electric field is applied, and  $\varepsilon_2(\omega)$  is related with absorption of the material. The imaginary part of interband contribution to the dielectric function is defined as

$$\varepsilon_2^{\alpha\beta}(\omega) = \frac{\hbar e^2}{\pi m^2 \omega^2} \sum_{cv} \int d\mathbf{k} \langle \Psi_{c\mathbf{k}} | p^{\alpha} | \Psi_{v\mathbf{k}} \rangle \langle \Psi_{v\mathbf{k}} | p^{\beta} | \Psi_{c\mathbf{k}} \rangle (f(\varepsilon_{c\mathbf{k}}) - f(\varepsilon_{v\mathbf{k}})) \delta(\varepsilon_{c\mathbf{k}} - \varepsilon_{v\mathbf{k}} - \omega). \quad (2.60)$$

Here,  $f$  is the Fermi distribution function,  $c$  and  $v$  are the indices of conduction band and valence band. The total imaginary part of dielectric function can be calculated when  $c$  and  $v$  run over all the conduction bands and valence bands. Similarly, the interband contribution can be achieved by calculating single conduction band and single valence band.

The real part of dielectric function can be calculated by Kramers-Kronig relations

$$\varepsilon_1^{\alpha\beta}(\omega) = \delta_{\alpha\beta} + \frac{2}{\pi} \mathbf{P} \int_0^\infty \frac{\omega' \varepsilon_2^{\alpha\beta}(\omega')}{\omega'^2 - \omega^2} d\omega'. \quad (2.61)$$

Here,  $\mathbf{P}$  the Cauchy principal value. The absorption coefficient can be obtained by the real part and imaginary part of dielectric function

$$\alpha^{ii}(\omega) = \frac{\sqrt{2}\omega}{c} \left[ \sqrt{\varepsilon_1^{ii}(\omega)^2 + \varepsilon_2^{ii}(\omega)^2} - \varepsilon_1^{ii}(\omega) \right]^{1/2}. \quad (2.62)$$

Here, the equation is only valid for the diagonal of the tensor.

In this section, only some basic equations are covered when it is related to calculate the dielectric function. If someone is interested in this topic, one can find more detailed in Ref. [104].

## 2.4 $\mathbf{k} \cdot \mathbf{p}$ method

The energy band dispersion can be obtained exactly by using the  $\mathbf{k} \cdot \mathbf{p}$  method in principle. The basic idea of this method is explained in this section [105, 106].

The non-relativistic Kohn-Sham equation (not in atomic units) is given as

$$\left( \frac{\mathbf{p}^2}{2m_e} + V(\mathbf{r}) \right) \Psi_{n,\mathbf{k}}(\mathbf{r}) = \epsilon_{n,\mathbf{k}} \Psi_{n,\mathbf{k}}(\mathbf{r}). \quad (2.63)$$

Here,  $\mathbf{p}$  is momentum operator, and the superscript "KS" is ignored compared with Eq. 2.37. According to the Bloch theory, the wavefunction can be written as

$$\Psi_{n,\mathbf{k}}(\mathbf{r}) = e^{i\mathbf{k}\mathbf{r}} u_{n,\mathbf{k}}(\mathbf{r}). \quad (2.64)$$

Here,  $u_{n,\mathbf{k}}(\mathbf{r})$  is a function which has the same periodicity as the potential. If substituting Eq. 2.64 to Eq. 2.63, the new equation is derived as

$$\left( \frac{\mathbf{p}^2}{2m_e} + V(\mathbf{r}) + \frac{\hbar^2 \mathbf{k}^2}{2m_e} + \frac{\hbar \mathbf{k} \mathbf{p}}{m_e} \right) u_{n,\mathbf{k}}(\mathbf{r}) = \epsilon_{n,\mathbf{k}} u_{n,\mathbf{k}}(\mathbf{r}). \quad (2.65)$$

In Eq. 2.65, the Hamiltonian becomes  $H_0 = \mathbf{p}^2/2m_e + V(\mathbf{r})$  when  $\mathbf{k} = \mathbf{0}$ , the corresponding eigenvalue is  $\epsilon_{n,\mathbf{0}}$ . Here, terms in  $H_0$  can be seen as non-perturbation terms, and remaining terms are seen as perturbation terms. From the perturbation theory, the following equation can be obtained

$$\epsilon_{n,\mathbf{k}} = \epsilon_{n,\mathbf{0}} + \frac{\hbar^2 \mathbf{k}^2}{2m_e} + \frac{\hbar^2}{m_e^2} \sum_n^N \sum_{n' \neq n}^N \frac{| \langle u_{n,\mathbf{0}}(\mathbf{r}) | \mathbf{k} \mathbf{p} | u_{n',\mathbf{0}}(\mathbf{r}) \rangle |^2}{\epsilon_{n,\mathbf{0}} - \epsilon_{n',\mathbf{0}}}. \quad (2.66)$$

In the realistic implementation, the following derivation is exploited [107]. Assume that the wavefunction and eigenvalue are obtained by some procedures on  $\mathbf{k}_0$  point.  $\Psi_{n,\mathbf{k}_0}(\mathbf{r})$  is the corresponding wavefunction and  $\epsilon_{n,\mathbf{k}_0}$  is the corresponding eigenvalue. Luttinger-Kohn function is given as

$$\chi_{n,\mathbf{k}}(\mathbf{r}) = e^{i(\mathbf{k}-\mathbf{k}_0)\mathbf{r}} \Psi_{n,\mathbf{k}_0}(\mathbf{r}). \quad (2.67)$$

The wavefunction on  $\mathbf{k}$  point can be expanded by  $\chi_{n,\mathbf{k}}(\mathbf{r})$ , which is given as

$$\Psi_{n,\mathbf{k}}(\mathbf{r}) = \sum_j^N C_{n,j}^{\mathbf{k}} \chi_{j,\mathbf{k}}(\mathbf{r}). \quad (2.68)$$

In Eq. 2.68, the wavefunction can be obtained if the coefficient  $C_{n,j}^{\mathbf{k}}$  is obtained. Based on Eq. 2.68 and Eq. 2.63, the following equation is derived

$$\begin{aligned} \sum_j^N C_{n,j}^{\mathbf{k}} \left( \left( \epsilon_{n,\mathbf{k}_0} - \epsilon_{n,\mathbf{k}} + \frac{\hbar^2}{2m_e} (\mathbf{k}^2 - \mathbf{k}_0^2) \right) \delta_{j',j} + \frac{\hbar}{m_e} (\mathbf{k} - \mathbf{k}_0) \bar{\mathbf{p}}_{j',j} \right) &= 0 \\ \bar{\mathbf{p}}_{j',j} &= \langle u_{j',\mathbf{k}_0}(\mathbf{r}) | \mathbf{p} | u_{j,\mathbf{k}_0}(\mathbf{r}) \rangle. \end{aligned} \quad (2.69)$$

Eq. 2.69 can be simplified as

$$\begin{aligned} \sum_j C_{n,j}^{\mathbf{k}} (H_{j',j} - \epsilon_{n,\mathbf{k}} \delta_{j',j}) &= 0 \\ H_{j',j} &= \left( \epsilon_{n,\mathbf{k}_0} + \frac{\hbar^2}{2m_e} (\mathbf{k}^2 - \mathbf{k}_0^2) \right) \delta_{j',j} + \frac{\hbar}{m_e} (\mathbf{k} - \mathbf{k}_0) \bar{\mathbf{p}}_{j',j}. \end{aligned} \quad (2.70)$$

Here, the coefficient  $C_{n,j}^{\mathbf{k}}$  and  $\epsilon_{n,\mathbf{k}}$  can be calculated. Therefore, the wavefunction on  $\mathbf{k}$  point can be obtained.

## 2.5 Spin-orbit coupling

### 2.5.1 Dirac equation

Non-relativistic quantum mechanics has broad application. However the non-relativistic quantum is not suitable to describe the system where the velocity of electron is near the one of light  $c$ . Therefore, Dirac introduced an equation which is called Dirac equation applying for relativistic case [108, 109].

Dirac defined the Hamiltonian as

$$H^{dirac} = c\boldsymbol{\alpha}\mathbf{P} + \beta m_e c^2 + V. \quad (2.71)$$

Here,  $\mathbf{P} = -i\hbar\nabla$  is the momentum operator,  $V$  is the general potential, and  $m_e$  is the mass of electron.  $\boldsymbol{\alpha}$  and  $\beta$  are  $4 \times 4$  matrices, which are defined as

$$\boldsymbol{\alpha} = \begin{pmatrix} 0 & \boldsymbol{\sigma} \\ \boldsymbol{\sigma} & 0 \end{pmatrix}, \beta = \begin{pmatrix} \mathbf{I} & 0 \\ 0 & -\mathbf{I} \end{pmatrix}. \quad (2.72)$$

Here,  $\mathbf{I}$  is unit matrix.  $\boldsymbol{\sigma}$  is Pauli matrix, which is given as

$$\boldsymbol{\sigma} = (\boldsymbol{\sigma}_x \ \boldsymbol{\sigma}_y \ \boldsymbol{\sigma}_z) \quad (2.73)$$

$$\boldsymbol{\sigma}_x = \begin{pmatrix} 0 & 1 \\ 1 & 0 \end{pmatrix}, \boldsymbol{\sigma}_y = \begin{pmatrix} 0 & -i \\ i & 0 \end{pmatrix}, \boldsymbol{\sigma}_z = \begin{pmatrix} 1 & 0 \\ 0 & -1 \end{pmatrix}. \quad (2.74)$$

### 2.5.2 Derivation of spin-orbit coupling

Assume that  $\Psi$  is the wavefunction of Hamiltonian in Eq. 2.71 which has four components [108, 109]. However, it can be written with only two terms

$$\Psi = \begin{pmatrix} \phi^\uparrow \\ \phi^\downarrow \\ \chi^\uparrow \\ \chi^\downarrow \end{pmatrix}, \Psi = \begin{pmatrix} \phi \\ \chi \end{pmatrix}. \quad (2.75)$$

Here,  $\phi$  includes the two terms of  $\phi^\uparrow$  and  $\phi^\downarrow$ , and  $\chi$  contains  $\chi^\uparrow$  and  $\chi^\downarrow$ . Under the non-relativistic limit,  $\phi$  is bigger than  $\chi$  by the ratio of  $v/c$ . Here,  $v$  and  $c$  are velocity of electron and light, respectively. Therefore, the  $\phi$  is considered as the large term and  $\chi$  is the small one.

In order to derive the spin-orbit coupling term, we need to take use of the non-relativistic limit approximation ( $v^2/c^2 \ll 1$ ). The time-independent Dirac equation is give as

$$E\Psi = (c\boldsymbol{\alpha}\mathbf{P} + \beta m_e c^2 + V)\Psi. \quad (2.76)$$

For convenience, the following equation is defined

$$E' = E - m_e c^2. \quad (2.77)$$

Here,  $E$  is the total energy,  $m_e c^2$  and  $E'$  are the rest mass energy and the remaining energy excluding the rest mass energy, respectively. Under the non-relativistic limit,  $E'$  is far smaller than  $m_e c^2$ . The following equation is given when Eq. 2.75 and Eq. 2.77 are put into Eq. 2.76

$$\begin{aligned} (E' - V)\Phi - c\boldsymbol{\sigma}\mathbf{P}\chi &= 0 \\ - c\boldsymbol{\sigma}\mathbf{P}\Phi + (E' + 2m_e c^2 - V)\chi &= 0. \end{aligned} \quad (2.78)$$

To eliminate the  $\chi$  (otherwise, it is the antiparticle problem), it ends up with the equation

$$\left( V + \frac{1}{2m_e}(\boldsymbol{\sigma}\mathbf{P})(1 + \frac{E' - V}{2m_e c^2})^{-1}(\boldsymbol{\sigma}\mathbf{P}) \right) \phi = E' \phi. \quad (2.79)$$

Here,  $E' - V$  is far smaller than  $2mc^2$ , therefore taking advantage of the Taylor expansion of it, as well as the following identites

$$\begin{aligned} [\mathbf{P}, V] &= -i\hbar\nabla V \\ (\boldsymbol{\sigma}\mathbf{A})(\boldsymbol{\sigma}\mathbf{B}) &= \mathbf{AB} + i\boldsymbol{\sigma}[\mathbf{A} \times \mathbf{B}]. \end{aligned} \quad (2.80)$$

The final equation is obtained under the non-relativistic limit

$$E'\phi = \left( \frac{\mathbf{P}^2}{2m_e} + V - \frac{\mathbf{P}^4}{8m_e^3c^2} - \frac{i\hbar}{4m_e^2c^2}(\nabla V)\mathbf{P} + \frac{\hbar}{4m_e^2c^2}\boldsymbol{\sigma}[\nabla V \times \mathbf{P}] \right) \phi. \quad (2.81)$$

Furthermore, we can approximate the above equation to the simpler expression under spherical symmetry potential

$$E'\phi = \left( \frac{\mathbf{P}^2}{2m_e} + V - \frac{\mathbf{P}^4}{8m_e^3c^2} - \frac{i\hbar}{4m_e^2c^2}(\nabla V)\mathbf{P} + \frac{1}{2m_e^2c^2} \frac{1}{R} \frac{dV}{dR} \mathbf{SL} \right) \phi. \quad (2.82)$$

Here,  $\mathbf{S} = \hbar\boldsymbol{\sigma}/2$  is the Pauli spinor, and  $\mathbf{L} = \mathbf{R} \times \mathbf{P}$  is the orbital angular momentum operator. The terms of  $\mathbf{P}^2/(2m_e) + V$  is Schrödinger term,  $\mathbf{P}^4/(8m_e^3c^2)$  and  $i\hbar(\nabla V)\mathbf{P}/(4m_e^2c^2)$  are the mass enhancement and Darwin term, respectively, both of them together is called the scalar relativistic approximation (SRA). The last term is the spin-orbit coupling (SOC) term. One has to notice that the Darwin term is not hermitian operator, alternatively,  $\nabla^2 V/(8m_e^2c^2)$  is suggested in the realistic implementation.

**Eq. 2.81** is only valid if the velocity of electrons is slower than the one of light. It is not true in the region which is close to the nucleus for heavy elements, where the relativistic effects are relatively strong. Moreover, the Coulomb potential can be arbitrarily large negative energies in realistic situation as well. Therefore, there is another way to derive the spin-orbit coupling which can overcome the mentioned disadvantages.

**Eq. 2.79** can be rewritten as

$$\begin{aligned} &\left( V + (\boldsymbol{\sigma}\mathbf{P}) \left( \frac{c^2}{2m_e c^2 - V} \right) \left( 1 + \frac{E'}{2m_e c^2 - V} \right)^{-1} (\boldsymbol{\sigma}\mathbf{P}) \right) \phi \\ &\approx \left( V + (\boldsymbol{\sigma}\mathbf{P}) \left( \frac{c^2}{2m_e c^2 - V} \right) (\boldsymbol{\sigma}\mathbf{P}) \right) \phi \\ &\quad - (\boldsymbol{\sigma}\mathbf{P}) \left( \frac{c^2}{2m_e c^2 - V} \right) \left( \frac{E'}{2m_e c^2 - V} \right)^{-1} (\boldsymbol{\sigma}\mathbf{P}) \phi + . \\ &= E'\phi. \end{aligned} \quad (2.83)$$

Here, the Taylor expansion is utilized. The zeroth order regular approximation (ZORA)

Hamiltonian [110–112] is defined as

$$\begin{aligned} H^{zora} &= V + (\boldsymbol{\sigma} \mathbf{P}) \left( \frac{c^2}{2m_e c^2 - V} \right) (\boldsymbol{\sigma} \mathbf{P}) \\ &= V + \mathbf{P} \left( \frac{c^2}{2m_e c^2 - V} \right) \mathbf{P} + \frac{c^2}{(2m_e c^2 - V)^2} \boldsymbol{\sigma} \cdot (\nabla V \times \mathbf{P}) \end{aligned} \quad (2.84)$$

The last term in Eq. 2.84 is the spin-orbit coupling term.

# Chapter 3

## Results and discussion

In this chapter, the major results for the licentiate thesis are discussed. The first one is parameterization of energy bands for  $\text{CuIn}_{1-x}\text{Ga}_x\text{Se}_2$  where  $x = 0, 0.5$ , and  $1$ . The second one is the calculation of the dielectric function spectra for the  $\text{CuIn}_{0.5}\text{Ga}_{0.5}\text{Se}_2$  by all electron and full-potential linearized augmented plane wave (FPLAPW) method, which is compared with experimental results. Moreover, the probable electronic origins of the critical point (CP) features are discussed as well.

### 3.1 Parameterization of energy bands for CIGS

#### 3.1.1 Parameterization method

The curvature of energy bands is often demonstrated by the effective electron and hole masses. Generally, the parabolic energy dispersion, also named parabolic band approximation (pba), is assumed to represent the shape of the energy bands

$$E_j^{pb}(\mathbf{k}) = E_j(\mathbf{0}) \pm \left[ \frac{\tilde{\mathbf{k}}_x^2 + \tilde{\mathbf{k}}_y^2}{m_j^\perp} + \frac{\tilde{\mathbf{k}}_z^2}{m_j^\parallel} \right] \quad (3.1)$$
$$\tilde{\mathbf{k}}_\alpha^2 = \frac{\hbar^2 \mathbf{k}_\alpha^2}{2e}, \text{ where } \alpha = x, y, \text{ and } z.$$

Here,  $m_j^\perp$  and  $m_j^\parallel$  are transverse electron masses and longitudinal electron masses, respectively. Parameters in Eq. 3.1 to describe the parabolic energy dispersions of the lowest conduction band (CB) and the three uppermost valence bands (VBs) in the vicinity of the  $\Gamma$ -point are given in **Table 3.1**.

Parameters	CuInSe <sub>2</sub>				CuIn <sub>0.5</sub> Ga <sub>0.5</sub> Se <sub>2</sub>				CuGaSe <sub>2</sub>			
	c1	v1	v2	v3	c1	v1	v2	v3	c1	v1	v2	v3
$E_j(\mathbf{0})$ [eV]	1.04	0	0.01	0.19	1.33	0	0.02	0.2	1.67	0	0.08	0.26
$m_j^\perp$ [ $m_0$ ]	0.08	0.14	0.25	0.27	0.10	0.40	0.17	0.29	0.13	0.47	0.20	0.29
$m_j^{\parallel}$ [ $m_0$ ]	0.09	0.66	0.12	0.28	0.11	0.14	0.61	0.40	0.13	0.15	0.61	0.49

**Table 3.1.** Parameters in Eq. 3.1 for CuInSe<sub>2</sub>, CuIn<sub>0.5</sub>Ga<sub>0.5</sub>Se<sub>2</sub>, and CuGaSe<sub>2</sub>.  $E_{v1}(\mathbf{0})$  is the valence band maximum (VBM) and  $E_{c1}(\mathbf{0})$  is the fundamental band-gap energy  $E_g$ .

Unfortunately, these effective masses are only valid around the considered  $\mathbf{k}$  point, which is not suitable to describe the non-parabolic away from this  $\mathbf{k}$  point. However, the accurate shape of energy bands is important when one simulates and analyzes the electron transport or band filling.

In this work, we have parameterized the three uppermost VBs and the lowest CB for the materials of CuInSe<sub>2</sub>, CuIn<sub>0.5</sub>Ga<sub>0.5</sub>Se<sub>2</sub>, and CuGaSe<sub>2</sub>. This parameterization is based on results from FPLAPW calculations. Normally, the  $\mathbf{k} \cdot \mathbf{p}$  method is utilized to parameterize the energy bands. However, the energy dispersions of CuIn<sub>1-x</sub>Ga<sub>x</sub>Se<sub>2</sub> where  $x = 0, 0.5$ , and  $1$  are rather complex due to the crystal-field interaction and the spin-orbit coupling. Therefore, the regular  $\mathbf{k} \cdot \mathbf{p}$  method is not sufficient to describe the energy bands. We manage to extend the  $\mathbf{k} \cdot \mathbf{p}$  expression to higher orders, which is called full band parameterization (fbp) in the following text. The fbp is valid around 0.5 eV below VBM and 0.5 eV above the conduction band minimum (CBM). The explicit equation is given as

$$\begin{aligned}
E_j(\mathbf{k}) = & E_j^{pb}(\mathbf{k}) + E_j^0 + \Delta_{j,1} \left( \delta_{j,1}^2 \left( \frac{\tilde{\mathbf{k}}_x^4 + \tilde{\mathbf{k}}_y^4}{m_0^2} \right) + \delta_{j,2}^2 \left( \frac{\tilde{\mathbf{k}}_x^2 \tilde{\mathbf{k}}_y^2}{m_0^2} \right) + 1 \right)^{1/2} \\
& + \Delta_{j,2} \left( \delta_{j,3}^3 \left( \frac{\tilde{\mathbf{k}}_x^6 + \tilde{\mathbf{k}}_y^6}{m_0^3} \right) + \delta_{j,4}^3 \left( \frac{\tilde{\mathbf{k}}_x^2 \tilde{\mathbf{k}}_y^4 + \tilde{\mathbf{k}}_x^4 \tilde{\mathbf{k}}_y^2}{m_0^3} \right) + 1 \right)^{1/3} \\
& + \Delta_{j,3} \left( \delta_{j,5}^2 \left( \frac{\tilde{\mathbf{k}}_z^4}{m_0^2} \right) + 1 \right)^{1/2} + \Delta_{j,4} \left( \delta_{j,6}^3 \left( \frac{\tilde{\mathbf{k}}_z^6}{m_0^3} \right) + 1 \right)^{1/3} \\
& + \Delta_{j,5} \left( \delta_{j,7}^2 \left( \frac{\tilde{\mathbf{k}}_x^2 \tilde{\mathbf{k}}_z^2 + \tilde{\mathbf{k}}_y^2 \tilde{\mathbf{k}}_z^2}{m_0^2} \right) + 1 \right)^{1/2} \\
& + \Delta_{j,6} \left( \delta_{j,8}^3 \left( \frac{\tilde{\mathbf{k}}_x^4 \tilde{\mathbf{k}}_z^2 + \tilde{\mathbf{k}}_y^4 \tilde{\mathbf{k}}_z^2}{m_0^3} \right) + \delta_{j,9}^3 \left( \frac{\tilde{\mathbf{k}}_x^2 \tilde{\mathbf{k}}_z^4 + \tilde{\mathbf{k}}_y^2 \tilde{\mathbf{k}}_z^4}{m_0^3} \right) + \delta_{j,10}^3 \left( \frac{\tilde{\mathbf{k}}_x^2 \tilde{\mathbf{k}}_y^2 \tilde{\mathbf{k}}_z^2}{m_0^3} \right) + 1 \right)^{1/3}. \tag{3.2}
\end{aligned}$$

Here,  $E_j^0$ ,  $\Delta_{j,n}$ , and  $\delta_{j,m}$  are fitting parameters (see Table. 3.2),  $m_0$  is the electron rest mass. In Eq. 3.2, each term represents one parabolic dispersion, the higher order terms

describe the larger wave vectors away from  $\Gamma$  point. Unfortunately, the complex energy dispersions requires many fitting parameters. However, the conduction band needs less fitting parameters.

### 3.1.2 Non-parabolicity properties

The fbp of  $\text{CuIn}_{1-x}\text{Ga}_x\text{Se}_2$  where  $x = 0, 0.5$ , and  $1$  are plotted compared with the pba (Eq. 3.1) as well as the calculations based on the FPLAPW method.

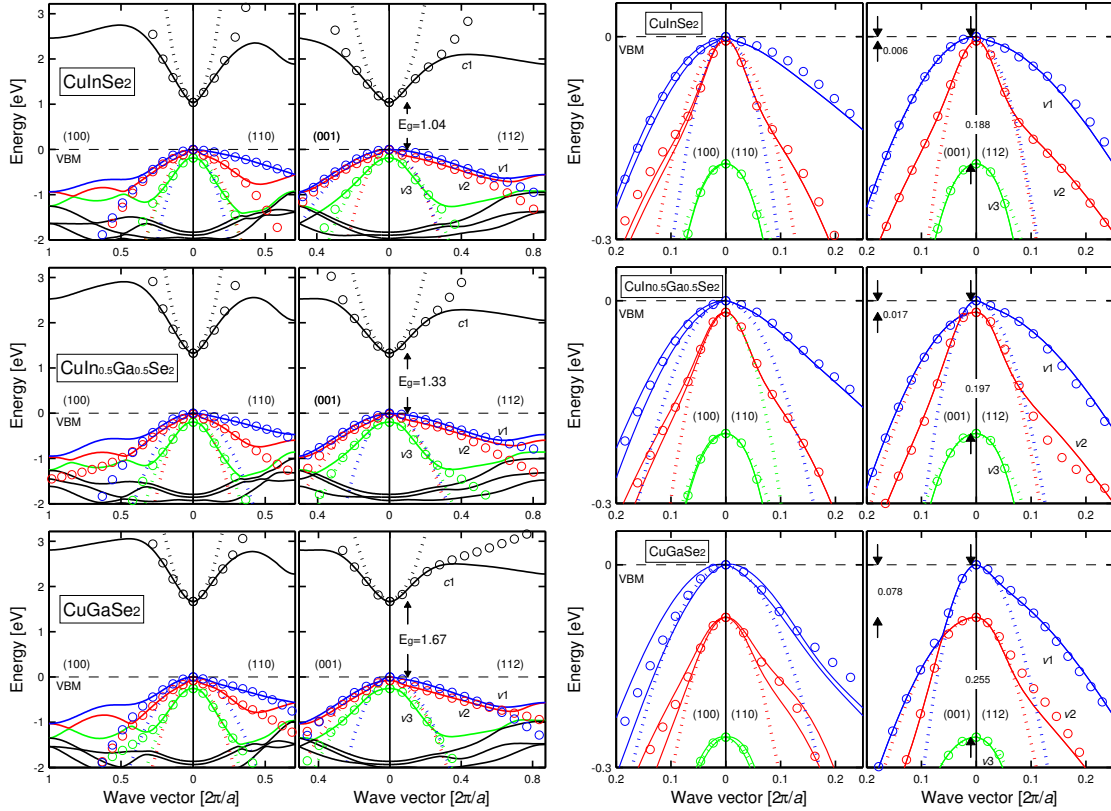


**Figure 3.1.** Left panel: Electronic band structure along four directions. The circles are the results of the full band parameterization (fbp), and the dotted lines represent the parabolic band approximation (pba). Right panel: The close-up of left panel for the valence bands close to  $\Gamma$  point.

In Fig. 3.1, the fbp can describe the energy below VBM around 0.5 eV accurately, and around 0.5 eV above the CB minimum (CBM) as well. However, the pba is only valid below VBM around  $-4$ ,  $-10$ , and  $-40$  meV for the  $\text{CuInSe}_2$ ,  $\text{CuIn}_{0.5}\text{Ga}_{0.5}\text{Se}_2$ , and  $\text{CuGaSe}_2$ , respectively. Since the lowest conduction band is more parabolic, therefore, the less fitting parameters are expected (see Table 3.2).

Parameters	CuInSe <sub>2</sub>			CuIn <sub>0.5</sub> Ga <sub>0.5</sub> Se <sub>2</sub>			CuGaSe <sub>2</sub>					
	<i>c1</i>	<i>v1</i>	<i>v2</i>	<i>v3</i>	<i>c1</i>	<i>v1</i>	<i>v2</i>	<i>v3</i>	<i>c1</i>	<i>v1</i>	<i>v2</i>	<i>v3</i>
$E_j^0$ [eV]	-4.010	-5.311	-5.242	-5.620	-4.146	-6.210	-6.426	-5.835	-3.927	5.284	-5.789	-2.783
$\Delta_{j,1}$ [eV]	-0.295	0.006	-0.002	-0.021	-0.230	0.106	1.321	-0.026	-0.454	0.116	1.284	-1.194
$\Delta_{j,2}$ [eV]	0	0.098	0.104	0.308	0	0.002	0.096	0.386	0	-10.771	-0.837	-0.024
$\Delta_{j,3}$ [eV]	-0.242	0.018	0.124	-0.025	-0.293	0.937	-0.017	-0.838	-0.419	0.088	0.347	-0.303
$\Delta_{j,4}$ [eV]	0	0.188	0.076	0.238	0	0.021	0.163	0.789	0	0.076	-0.051	0.608
$\Delta_{j,5}$ [eV]	-0.016	-0.048	0.001	-0.009	-0.046	0.001	0.011	0.37	-0.047	0.022	0.274	0.374
$\Delta_{j,6}$ [eV]	0	0.037	-0.073	0.117	0	-0.022	-0.313	-0.012	0	-0.111	-0.525	-4.362
$\delta_{j,1}$ [eV <sup>-1</sup> ]	30.669	952	2304.147	94.139	27.157	5.517	1.029	57.007	11.865	10.526	9.269	3.839
$\delta_{j,2}$ [eV <sup>-1</sup> ]	47.374	1754.386	4587.156	220.556	44.506	13.61	0.413	153.435	20.262	28.545	21.582	6.232
$\delta_{j,3}$ [eV <sup>-1</sup> ]	0	3.97	72.296	11.746	0	487.805	46.95	8.489	0	0.131	9.116	59.625
$\delta_{j,4}$ [eV <sup>-1</sup> ]	0	3.688	123.274	18.078	0	1128.668	72.844	13.509	0	0.126	21.328	148.516
$\delta_{j,5}$ [eV <sup>-1</sup> ]	31.852	6.041	56.004	64.137	21.124	1.314	247.158	7.921	12.978	7.709	12.141	8.014
$\delta_{j,6}$ [eV <sup>-1</sup> ]	0	3.134	6.1	12.031	0	267.523	29.076	8.743	0	64.185	66.808	5.309
$\delta_{j,7}$ [eV <sup>-1</sup> ]	222.641	37.004	3846.154	206.148	79.879	3322.259	212.902	16.836	76.319	236.742	16.24	5.092
$\delta_{j,8}$ [eV <sup>-1</sup> ]	0	12.647	16.269	6.982	0	92.954	4.885	57.89	0	31.947	6.71	1.209
$\delta_{j,9}$ [eV <sup>-1</sup> ]	0	61.565	33.169	34.114	0	118.064	0	273.4	0	34.784	4.831	1.394
$\delta_{j,10}$ [eV <sup>-1</sup> ]	0	46.679	31.275	32.237	0	110.327	6.074	153.523	0	40.765	5.243	2.124

**Table 3.2.** Parameters in Eq. 3.2 to describe the non-parabolic contribution to the energy dispersions  $E_j(\mathbf{k})$  of the lowest CB and the three uppermost VBs. The notation of the energy bands ( $j = c1, v1, v2$ , and  $v3$ ) refers to a spin-independent band indexing, where  $c1$  represents the bottommost CB and  $v1$  represents the topmost valence band (VB).

To further utilize this parameterization method, the energy dispersions of the lowest CB and the three uppermost VBs are parameterized for kesterite and stannite  $\text{Cu}_2\text{ZnSnS}_4$  and  $\text{Cu}_2\text{ZnSnSe}_4$  as well. It works as good as  $\text{CuInSe}_2$ ,  $\text{CuIn}_{0.5}\text{Ga}_{0.5}\text{Se}_2$ , and  $\text{CuGaSe}_2$ . Therefore, this parameterization method can be utilized to other materials potentially.

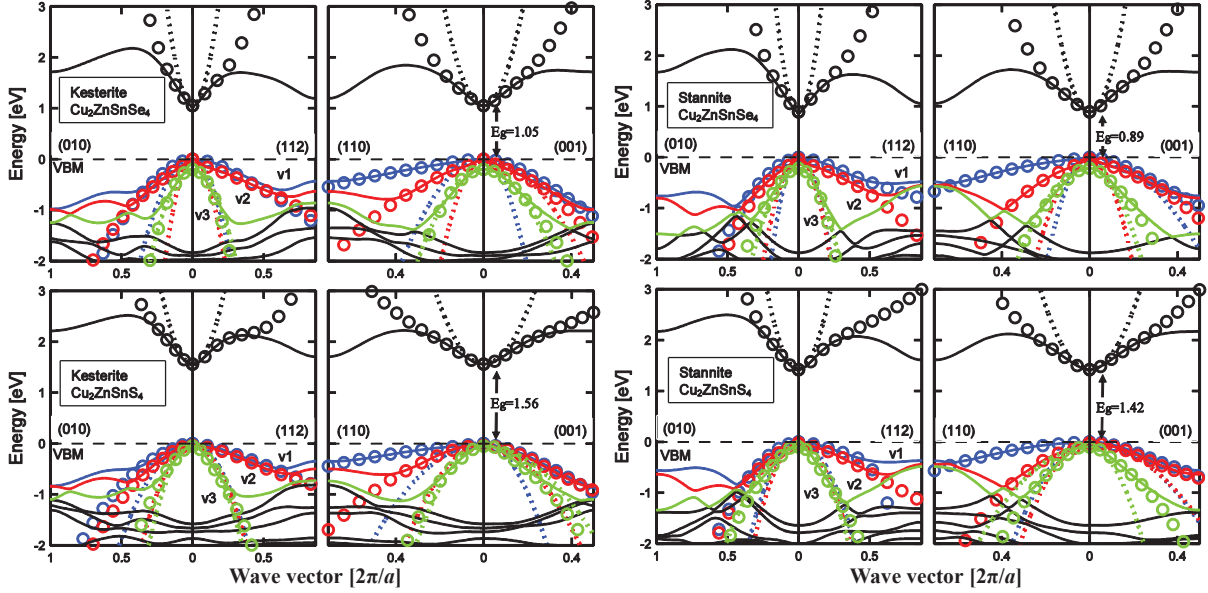


**Figure 3.2.** Left panel: electronic band structure for the kesterite structures of  $\text{Cu}_2\text{ZnSnS}_4$  and  $\text{Cu}_2\text{ZnSnSe}_4$ . Right panel: electronic band structure of the stannite structures of  $\text{Cu}_2\text{ZnSnS}_4$  and  $\text{Cu}_2\text{ZnSnSe}_4$ . The circles are the results based on the fbp, and the dotted lines represent results based on the pba.

In order to demonstrate the anisotropic and non-parabolic of energy bands further, the constant energy surface  $S_j(E)$  is determined for  $\text{CuInSe}_2$  and  $\text{CuGaSe}_2$ .

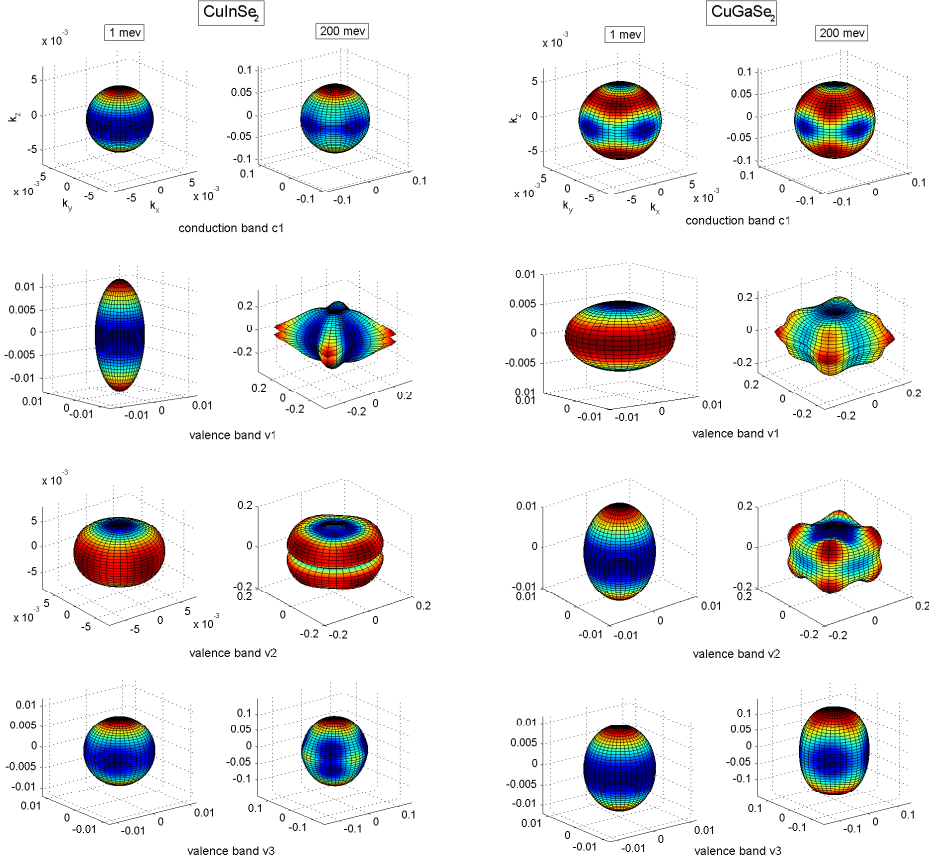


**Figure 3.3.** Left panel: constant energy surfaces for the three uppermost VBs and the lowest CB for the energies  $E = 1$  meV. Right panel: constant energy surfaces for the three uppermost VBs and the lowest CB for the energies  $E = 200$  meV.

In Fig. 3.3, it is near to  $\Gamma$  point when it refers to 1 meV; it is far away the  $\Gamma$  point when it refers to 200 meV. One notices that the pba is proper to describe the energy bands close to the  $\Gamma$  point, and it is ellipsoidal shaped sphere. For example, for the topmost VB ( $v_1$ ) of CuInSe<sub>2</sub>, the constant energy surface is ellipsoidal in the vicinity of the  $\Gamma$  point since the effective masses are anisotropic ( $m_{v1}^{\perp} = 0.14m_0$  and  $m_{v1}^{\parallel} = 0.66m_0$  in Table 3.1). However, the constant energy surface becomes non-ellipsoidal when the energies is far away from  $\Gamma$  point. For example, for the same band, the constant energy surface is not ellipsoidal shape at all when the energies goes up to 200 meV. It also implies that it is not correct to consider the constant effective mass. The change is relatively small for the CB.

### 3.1.3 Application of the full band parameterization

The parameterized energy bands can be exploited to reveal the detailed information near the VB and CB edged. In this section, the effective masses, density-of-states (DOS), Fermi level, and carrier concentration are calculated based on fbp. In comparison with the results based on pba, all of the corresponding results are calculated with the pba as well.

The effective masses are  $\mathbf{k}$ -independent for the pba, which is not fully correct due to the non-parabolicity and anisotropy of the energy bands. The effective masses tensors are calculated numerically by  $m_j(\mathbf{k}) = \pm \hbar^2 / (\partial^2 E_j(\mathbf{k}) / \partial \mathbf{k}^2)$  where  $j = c1, v1, v2$ , and  $v3$ .

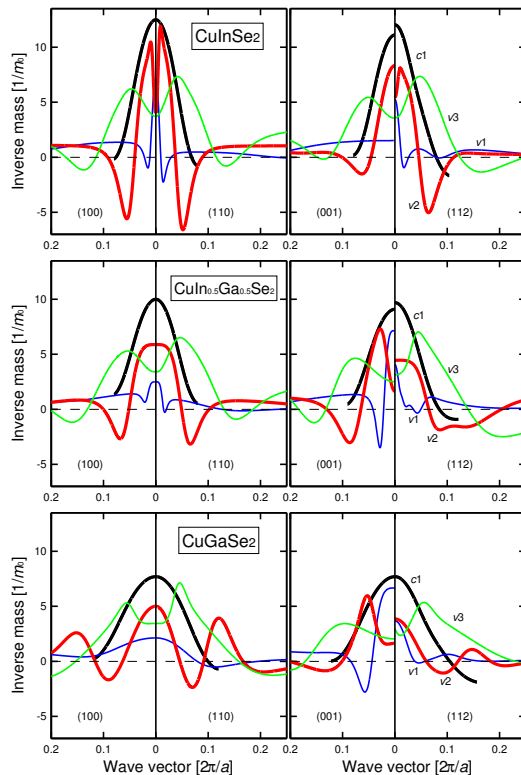


**Figure 3.4.** Inverse of the effective electron and hole masses in the four symmetry directions for the  $\text{CuIn}_{1-x}\text{Ga}_x\text{Se}_2$  ( $x = 0, 0.5$ , and  $1$ ).

In Fig. 3.4, it demonstrates that the energy bands of  $\text{CuIn}_{1-x}\text{Ga}_x\text{Se}_2$  ( $x = 0, 0.5$ , and  $1$ ) are strong non-parabolic, since the effective masses should be constant in the pba along each symmetry direction. The effective hole masses of the two topmost VBs are strong anisotropy close to the  $\Gamma$  point. However, the electron masses of conduction bands are rather isotropic ( $m_{c1}^{100}(\mathbf{0}) \approx m_{c1}^{110}(\mathbf{0}) \approx m_{c1}^{001}(\mathbf{0}) \approx m_{c1}^{112}(\mathbf{0})$ ). Hole masses of  $\text{CuGaSe}_2$  vary somewhat less compared with those of  $\text{CuInSe}_2$  because  $\text{CuGaSe}_2$  has larger split between the VBs. The inverse of the mass are presented in order to better visibility.

In order to further analyze the impact of non-parabolicity and anisotropy of the energy bands, the DOS is calculated based on fba and pba. The DOS in  $j$ th band is defined as

$$g_j(E) = \frac{1}{\Omega} \sum_{\mathbf{k}} 2\delta(E - E_j(\mathbf{k})) = \frac{1}{4\pi^3} \int_{E_j(\mathbf{k})=E} \frac{dS(\mathbf{k})}{|\nabla_{\mathbf{k}} E_j(\mathbf{k})|}. \quad (3.3)$$

Here,  $E_j(\mathbf{k}) = E$  is the  $\mathbf{k}$  space surface with constant energy  $E$ , and the  $\nabla_{\mathbf{k}} E_j(\mathbf{k})$  is the gradient of the energy dispersion. In the case of the pba, Eq. 3.3 can be written as

$$g_j^{pba}(E) = \frac{1}{2\pi^2} \left( \frac{2m_j^{DOS}}{\hbar^2} \right)^{3/2} \sqrt{|E - E_j(\mathbf{0})|}. \quad (3.4)$$

Here, the DOS mass  $m_j^{DOS}$  is equal to  $(m_j^\perp m_j^\perp m_j^\parallel)^{1/3}$ , which represents the extent of filling the specific band with free carriers to certain energy. In order to take advantage of the simple Eq. 3.4 for the non-parabolic energy bands, the energy-dependent DOS mass ( $m_{v/c}^{DOS}$ ), which contains the non-parabolicity and anisotropy of the band dispersion, is defined as

$$g_{v/c}(E) = \sum_j g_j(E) = \frac{1}{2\pi^2} \left( \frac{2m_{v/c}^{DOS}(E)}{\hbar^2} \right)^{3/2} \sqrt{|E - E_{v1/c1}(\mathbf{0})|}. \quad (3.5)$$

Here, the energy-dependent DOS mass  $m_{v/c}^{DOS}(E)$  contains the non-parabolicity and anisotropy of the band dispersion.

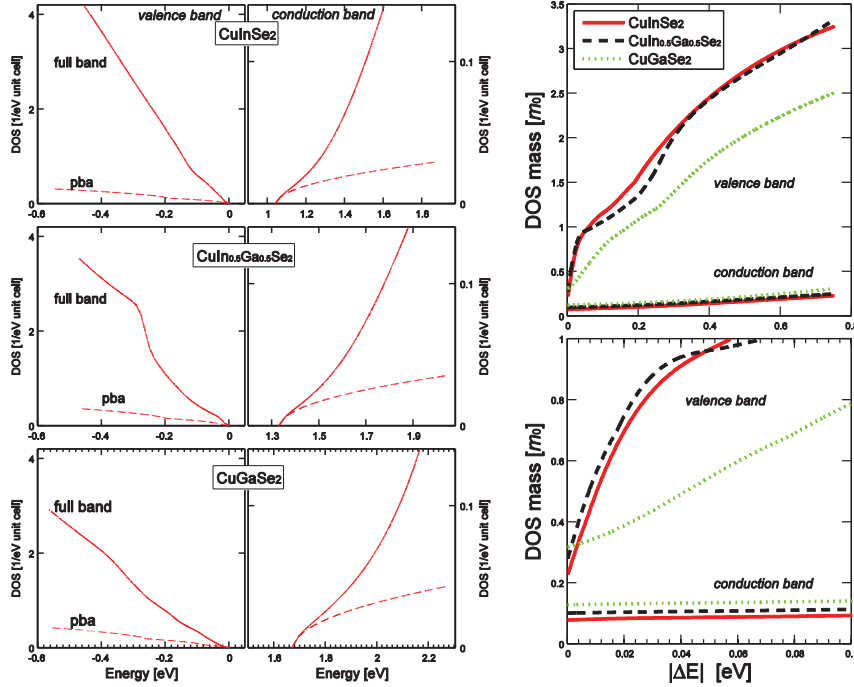


**Figure 3.5.** Left panel: total DOS of the VBs and CB. The solid lines show the results based on the fbp, and the dashed lines represent the results based on the pba. Right panel: The DOS mass  $m_{v/c}^{DOS}$  is calculated from Eq. 3.5.

Left panel in Fig. 3.5 demonstrates that the non-parabolicity of the bands strongly affect the DOS dispersions. The difference is remarkable. The fbp always generates larger DOS, the reason is that the non-parabolic energy bands are more flat than parabolic bands. Right panel in Fig. 3.5 demonstrates that the DOS masses of CuIn<sub>1-x</sub>Ga<sub>x</sub>Se<sub>2</sub> ( $x = 0, 0.5$ , and  $1$ ) is strong energy dependence with the VB DOS mass, which proves further the importance of considering non-parabolicity and anisotropy of the energy bands, especially for the VBs. For example, the effective mass of topmost VB for CuInSe<sub>2</sub> is around  $0.23 m_0$  close to the  $\Gamma$  point, which goes up to around  $1.00 m_0$  when  $E$  is around 0.1 eV. However, the change in the CB DOS mass is subtle, but also goes up to 2–3 times with respect to the value around  $\Gamma$  point.

The concentration of free holes  $n_v(T)$  and free electrons  $n_c(T)$  can be calculated from the DOS by

$$\begin{aligned} n_v(T) &= \int_{-\infty}^{E_{v1}(0)} g_v(E)(1 - f(E))dE \\ n_c(T) &= \int_{E_{c1}(0)}^{\infty} g_c(E)f(E)dE. \end{aligned} \quad (3.6)$$

Here,  $f(E) = 1/[1 + \exp(E - E_F)/k_B T]$  is the Fermi distribution function. The intrinsic carrier concentration can be expressed as

$$n_i(T) = \sqrt{n_c(T) \cdot n_v(T)}. \quad (3.7)$$

The extrinsic carrier concentration for *p*-type materials can be derived as:

$$n_v(T) = \frac{n_i^2(T)}{n_v(T)} + \sum_{\alpha} \frac{N_{A_{\alpha}}}{1 + g_{A_{\alpha}} e^{(\Delta_{A_{\alpha}} - E_F)/k_B T}}. \quad (3.8)$$

Here,  $N_{A_{\alpha}}$  is the acceptor concentration of the  $\alpha$ th defect,  $\Delta_{A_{\alpha}}$  implies the energy level of the acceptor state, and the  $g_{A_{\alpha}}$  is the spin degeneracy factor. The measured ionization energies for V<sub>Cu</sub> are utilized from Ref. [113].

The free carrier concentration in intrinsic for CuIn<sub>1-x</sub>Ga<sub>x</sub>Se<sub>2</sub> ( $x = 0, 0.5$ , and  $1$ ) is obtained considering the temperature dependency of the band gaps (Eq. 3.9) [114]. The results from the pba for silicon (Si) and gallium arsenide (GaAs) are compared with our calculation as well.

$$E_g(T) = E_g(0) - \frac{a \cdot T^2}{b + T}. \quad (3.9)$$

Here, parameters  $a$  and  $b$  are exploited from experimental values.

Parameters	CuInSe <sub>2</sub>	CuIn <sub>0.5</sub> Ga <sub>0.5</sub> Se <sub>2</sub>	CuGaSe <sub>2</sub>
$a$ [eV·K <sup>-1</sup> ]	1.086	3.000	2.017
$b$ [K]	97	277	209

Table 3.3. Parameters of  $a$  and  $b$  in Eq. 3.9

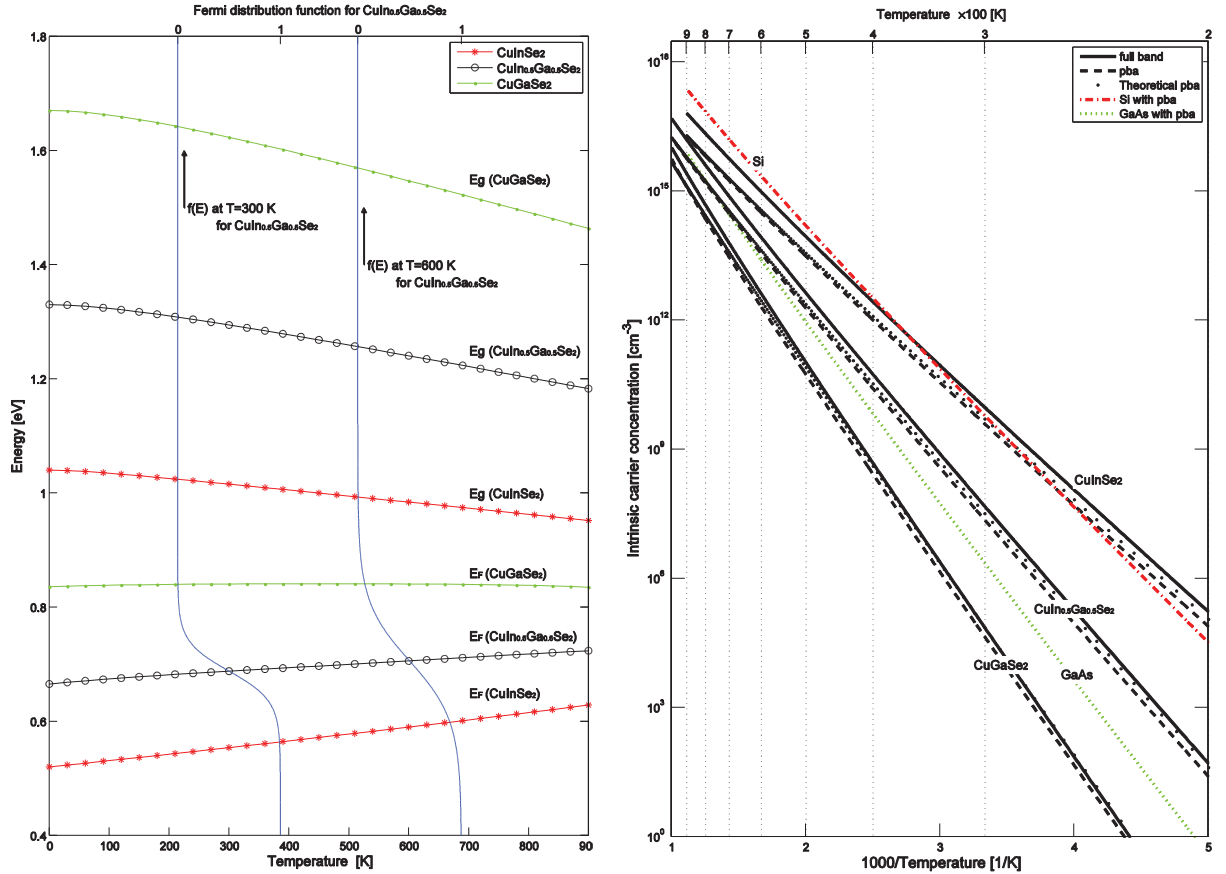


**Figure 3.6.** Left panel: Band-gap energy  $E_g$  and Fermi energy  $E_F$  for  $1 \leq T \leq 900$  K of intrinsic  $\text{CuInSe}_2$ ,  $\text{CuIn}_{0.5}\text{Ga}_{0.5}\text{Se}_2$ , and  $\text{CuGaSe}_2$ , determined from the fbp. In this figure, we also present the Fermi distribution  $f(E)$  of  $\text{CuIn}_{0.5}\text{Ga}_{0.5}\text{Se}_2$  for  $T = 300$  K and  $600$  K. Right panel: Intrinsic carrier concentration as function of temperature. For comparison, the theoretical results for GaAs and Si using the pba are given.

In Fig. 3.6, the temperature dependent band-gap and Fermi level (left panel) and intrinsic carrier concentration (right panel) are shown. In the left panel of Fig. 3.6, the band-gap is 1.04, 1.33, and 1.67 eV for the  $\text{CuIn}_{1-x}\text{Ga}_x\text{Se}_2$  where  $x = 0, 0.5$ , and  $1$  at temperature around 0 K, respectively. Fermi level is exactly the mid-gap energy. The Fermi level changes only slightly with temperature. However, for  $\text{CuInSe}_2$  and  $\text{CuIn}_{0.5}\text{Ga}_{0.5}\text{Se}_2$ , the Fermi levels increase somewhat more compared with  $\text{CuGaSe}_2$ . This is primarily because the CB of DOS mass for  $\text{CuGaSe}_2$  is almost the same, but the VB of DOS mass for  $\text{CuGaSe}_2$  change smaller compared with  $\text{CuInSe}_2$  and  $\text{CuIn}_{0.5}\text{Ga}_{0.5}\text{Se}_2$  which will affect the DOS. As a consequence, the Fermi level is closer to the CB minimum in the In rich compounds. At  $T = 300$  K and  $600$  K, the band-gap energies  $E_g$  and Fermi energy  $E_F$  are given in Table 3.4

	CuInSe <sub>2</sub>	CuIn <sub>0.5</sub> Ga <sub>0.5</sub> Se <sub>2</sub>	CuGaSe <sub>2</sub>
$E_g$ 300 K [eV]	1.02	1.29	1.62
$E_g$ 600 K [eV]	0.98	1.24	1.55
$E_F$ 300 K [eV]	0.55	0.69	0.84
$E_F$ 600 K [eV]	0.59	0.71	0.84

**Table 3.4.** Band-gap energies  $E_g$  and Fermi energy  $E_F$  at 300 K and 600 K, respectively.

In the left panel of **Fig. 3.6**, the Fermi distribution of CuIn<sub>0.5</sub>Ga<sub>0.5</sub>Se<sub>2</sub> is given at 300 K and 600 K, respectively. The probability of occupying the VBM (CBM) by a hole (an electron) is relative increase of around  $10^6$  times from 300 K to 600 K. In the right panel of **Fig. 3.6**, the intrinsic carrier concentration is increased dramatically with the increasing of temperature for the CuIn<sub>1-x</sub>Ga<sub>x</sub>Se<sub>2</sub> where  $x = 0, 0.5$ , and  $1$ . For example, in the case of CuInSe<sub>2</sub>, the carrier concentration is increased up to around  $10^5$  times higher from temperature 300 K to 600 K. The intrinsic carrier concentration for the Si and CuInSe<sub>2</sub> are rather comparable. The free carrier concentration is increased goes up to 2–3 times by taking into account the non-parabolicity of the energy bands.

Since as-grown CIGS typically has *p*-type character, the Fermi level and *p*-type carrier concentration of free holes  $n_v(T)$  and free electrons  $n_c(T)$  are calculated by assuming the presences of the native Cu vacancies as acceptors.

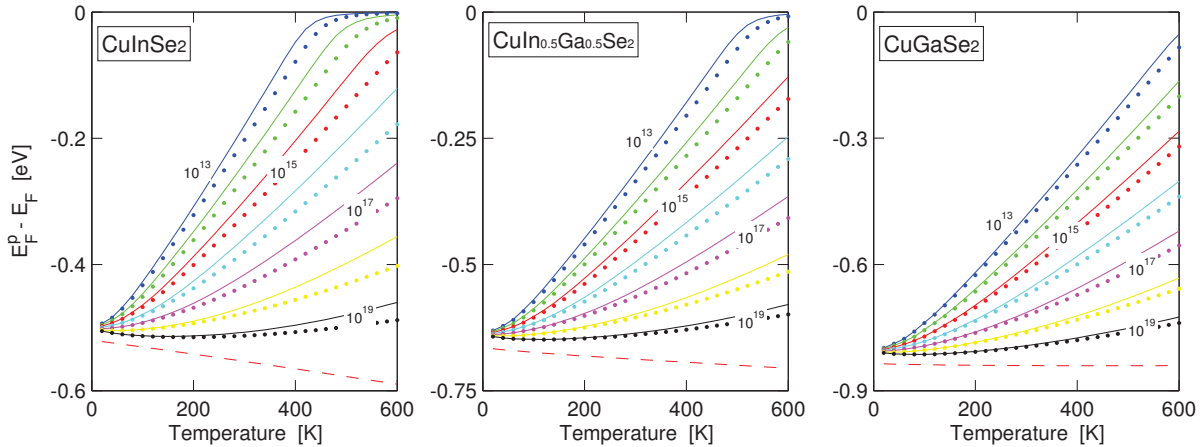


**Figure 3.7.** Fermi level as function of the temperature  $20 \leq T \leq 600$  of *p*-type CuInSe<sub>2</sub>, CuIn<sub>0.5</sub>Ga<sub>0.5</sub>Se<sub>2</sub>, and CuGaSe<sub>2</sub> for the effective doping concentration  $N_A = 10^{13}, 10^{14}, 10^{15}, ., \text{ and } 10^{19} \text{ acceptors cm}^{-3}$ . The energy scale  $E_F^P - E_F$  describes the Fermi energy with respect to the intrinsic  $E_F$  (**Fig. 3.6**). Dashed lines represent the VBM with respect to the intrinsic Fermi level. Solid and dotted lines represents the fbp and the pba, respectively.

The calculated Fermi level  $E_F^P$  in *p*-type materials is presented in **Fig. 3.7**, referred to the

Fermi level of the intrinsic materials  $E_F$  from **Fig. 3.6**. Only at very high temperatures ( $T > 400K$ ) and for low acceptor concentrations, the Fermi level of *p*-type  $\text{CuIn}_{1-x}\text{Ga}_x\text{Se}_2$  where  $x = 0, 0.5$ , and  $1$  can reach the Fermi level of corresponding intrinsic compounds. Moreover, although the different compounds have comparable acceptor ionization energies, the Ga rich alloy has lower relative Fermi level; this is a direct consequence of the larger band-gap of the Ga rich alloy. By comparing the calculations with the pba (dotted lines in **Fig. 3.7**) and the fba (solid lines) for each of the three  $\text{CuIn}_{1-x}\text{Ga}_x\text{Se}_2$  where  $x = 0, 0.5$ , and  $1$  alloys. One notices that the Fermi level is similar for the two models only at low and at very high temperatures. In the mid-temperature region the difference is however apparent.

The *p*-type carrier concentration (**Fig. 3.8**) for  $\text{CuIn}_{1-x}\text{Ga}_x\text{Se}_2$  ( $x = 0, 0.5$ , and  $1$ ) is presented using **Eq. 3.8**

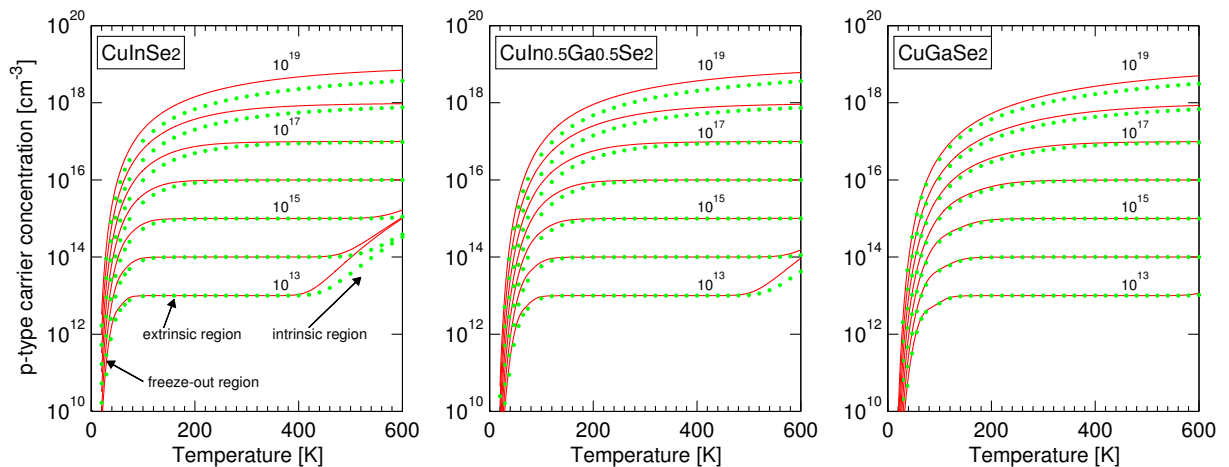


**Figure 3.8.** Free carrier concentration as function of the temperature in *p*-type for  $\text{CuInSe}_2$ ,  $\text{CuIn}_{0.5}\text{Ga}_{0.5}\text{Se}_2$ , and  $\text{CuGaSe}_2$ . The effective doping concentration  $N_A = 10^{13}, 10^{14}, 10^{15}, \dots$ , and  $10^{19}$  acceptors  $\text{cm}^{-3}$  are considered.

In **Fig. 3.8**, the carrier concentration is recognized by three different regions: the freeze-out region, the extrinsic region and the intrinsic region. The transition from the freeze-out region to the extrinsic region happens below the room temperature except that the uncompensated acceptor concentration is above around  $10^{18} \text{ cm}^{-3}$ . The transition from the extrinsic region to the intrinsic region for In rich compounds occurs at the lower temperature since they have smaller band gaps. The result based on the pba underestimates the carrier concentration around by the factor of 2 in the both freeze-out and intrinsic

regions. Therefore, the non-parabolic energy bands is required in order to describe the carrier concentration more accurately.

### 3.2 Dielectric function for $\text{CuIn}_{0.5}\text{Ga}_{0.5}\text{Se}_2$

The dielectric function ( $\varepsilon(\omega) = \varepsilon_1(\omega) + i\varepsilon_2(\omega)$ ) spectra of  $\text{CuIn}_{0.5}\text{Ga}_{0.5}\text{Se}_2$  is calculated by the all electron and full-potential linearized augmented plane wave (FPLAPW) method. The calculated dielectric function is compared with experimental values ( $\text{CuIn}_{0.7}\text{Ga}_{0.3}\text{Se}_2$ ) at temperature of 40 K and 300 K. They are in a good agreement. The different contributions to  $\varepsilon_2(\omega)$  in terms of the transitions between the valence bands and the conduction bands are identified based on this calculation. Moreover, the  $\mathbf{k}$ -dependence of the interband critical points (CPs) along the main symmetry directions is analyzed as well.

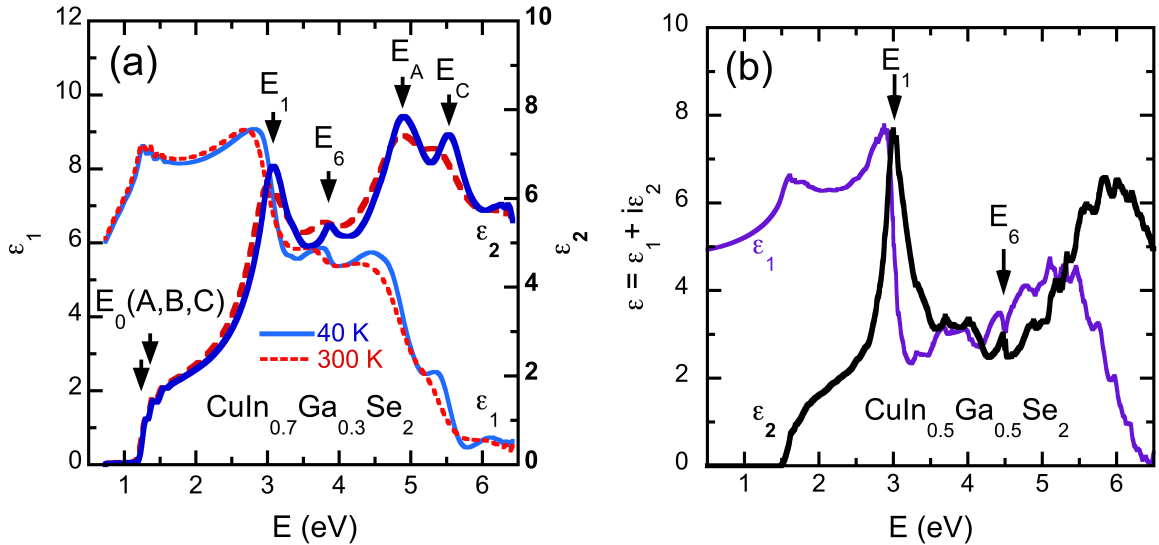


**Figure 3.9.** Left panel: The real ( $\varepsilon_1$ ) and imaginary ( $\varepsilon_2$ ) part of dielectric function spectra for  $\text{CuIn}_{0.7}\text{Ga}_{0.3}\text{Se}_2$  at 40 K (solid blue line) and 300 K (dashed red lines). Four prominent CP features are shown. Right panel: the dielectric function spectra for  $\text{CuIn}_{0.5}\text{Ga}_{0.5}\text{Se}_2$  calculated by FPLAPW method at 0 K. The major CP features are identified.

In Fig. 3.9, the general shape between experimental and calculated dielectric function is relatively similar. The calculation indicates that there is no big difference in the optical properties for those two materials, except the shift of CP energies. The analysis based on experimental work indicates that there are twelve CPs from 2.5 eV to 6.4 eV. Therefore, the electronic origin for each CP is analyzed based on the calculated results. The contribution to dielectric function between the valence bands and conduction bands is presented as well in Fig. 3.10.

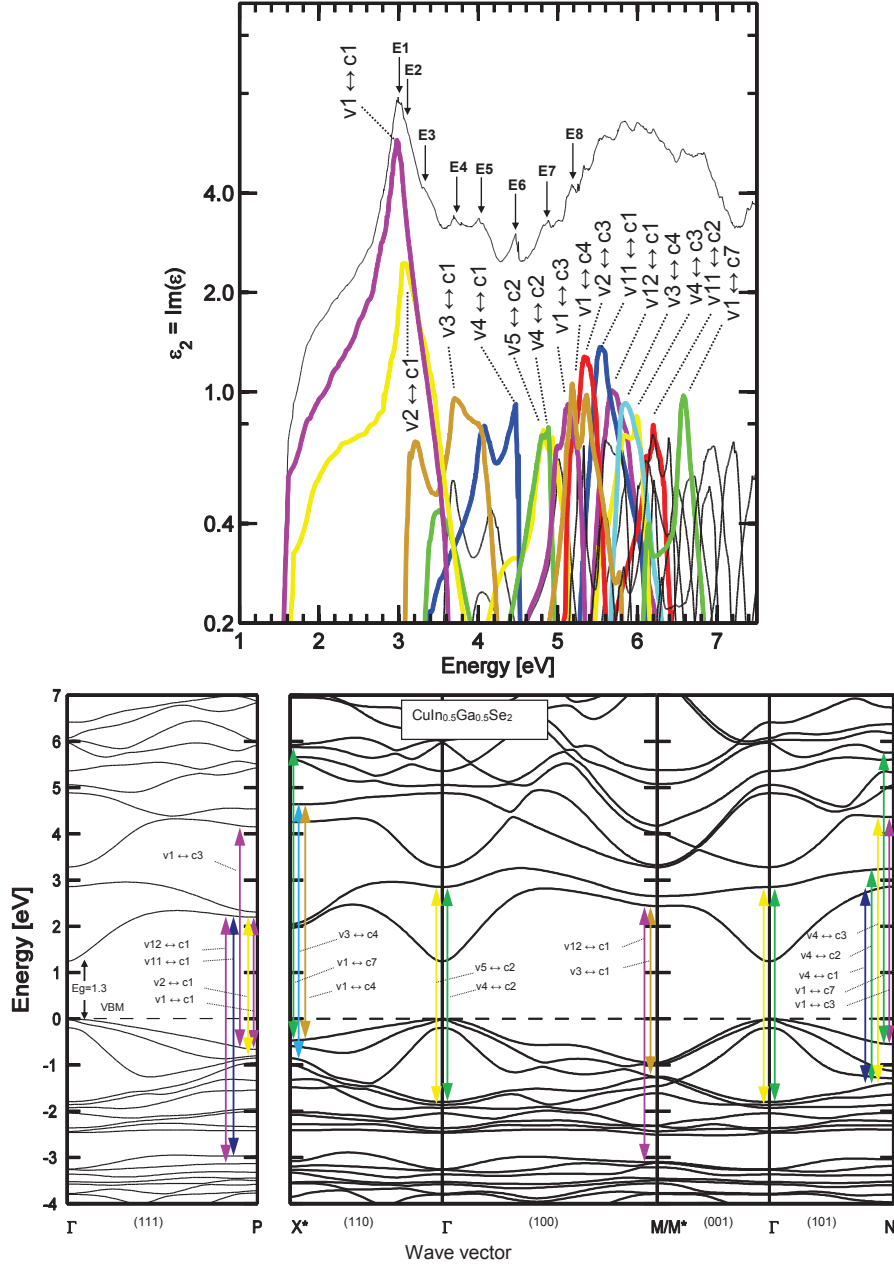


**Figure 3.10.** Upper panel: band-to-band analysis of the contribution to the total  $\varepsilon_2$  spectrum. The vertical axis is in the log scale. lower panel: the calculated electronic band structure of  $\text{CuIn}_{0.5}\text{Ga}_{0.5}\text{Se}_2$  where the CPs are identified along the main symmetry directions.

Here,  $v_1$  and  $c_1$  represent the topmost valence band and lowest conduction band, respectively. From Fig. 3.10, one notices that the  $E_1$  CP comes from the  $v_1 \rightarrow c_1$  transition near the  $P(1/2, 1/2, 1/2)$  point of the Brillouin zone (BZ). The  $E_2$  and  $E_3$  CPs are cor-

responding to transition of  $v_2 \rightarrow c_1$  in the P point as well in the BZ. The  $E_2$  and  $E_3$  CPs are small peak in the **Fig. 3.10**. However, the calculation of CuInSe<sub>2</sub> indicates that they happens 0.1–0.2 eV higher than the  $E_1$  CP, which is distinct spectral features (**Fig. 3.11**). The  $E_4$  CP comes from the transition of  $v_3 \rightarrow c_1$  at the  $M(1, 0, 0) = M^*(0, 0, 1)$  point. The  $E_5$  CP is contributed by the transitions  $v_4 \rightarrow c_1$  at the  $N(1/2, 0, 1/2)$  point and  $v_3 \rightarrow c_1$  at the  $M/M^*$  point. The  $E_6$  CP feature corresponding to the  $v_4 \rightarrow c_1$  at the N point. The  $E_7$  is from the transitions  $v_4 \rightarrow c_2$  at the  $\Gamma(0, 0, 0)$  and N point, the  $v_5 \rightarrow c_2$  at the  $\Gamma$  point is also contributed.

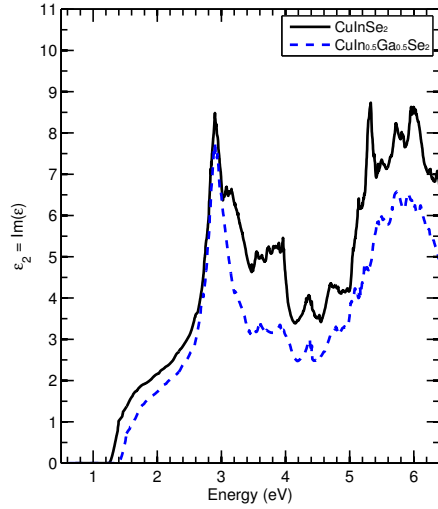


**Figure 3.11.** The  $\varepsilon_2$  spectra for CuInSe<sub>2</sub> and CuIn<sub>0.5</sub>Ga<sub>0.5</sub>Se<sub>2</sub>.

# Chapter 4

## Summary of the publications

### I Parameterization of $\text{CuIn}_{1-x}\text{Ga}_x\text{Se}_2$ ( $x = 0, 0.5$ , and $1$ ) energy bands

R. Chen and C. Persson, *Thin Solid Films* **519**, 7503 (2011).

We have parameterized the electronic band structure of  $\text{CuIn}_{1-x}\text{Ga}_x\text{Se}_2$  ( $x = 0, 0.5$ , and  $1$ ). It demonstrates that the energy dispersions of the lowest conduction band and three uppermost valence bands are strongly anisotropic and non-parabolic close to the  $\Gamma$ -point. This anisotropy and non-parabolicity directly affect the effective electron and hole masses.

### II Band-edge density-of-states and carrier concentrations in intrinsic and *p*-type $\text{CuIn}_{1-x}\text{Ga}_x\text{Se}_2$

R. Chen and C. Persson, *J. Appl. Phys.* **112**, 103708 (2012).

We have analyzed the energy band dispersion and the carrier concentration in chalcopyrite  $\text{CuIn}_{1-x}\text{Ga}_x\text{Se}_2$  ( $x = 0, 0.5$ , and  $1$ ) alloys. The overall results are: (i) the three uppermost valence bands (VBs) are strongly anisotropic and non-parabolic. (ii) The lowest CB becomes non-parabolic for energies 50–100 meV above the  $\Gamma$ -point band minimum. (iii) A constant density-of-states (DOS) mass cannot accurately describe band filling of the valence bands even at low hole concentrations. Instead, we introduce an energy dependent DOS mass that can be utilized to describe the carrier concentration and the Fermi energy using traditional equations for the DOS. (iv) With the full description of the energy dispersion, the hole concentration is improved by a factor of 10–50 and the electron concentration is improved by a factor of 2–10 depending on quasi-Fermi energy. (v) The transition from the freeze-out region to the extrinsic region occurs well below the room temperature for uncompensated acceptor concentration below around  $10^{17} \text{ cm}^{-3}$ , whereas for higher concentrations, not all acceptors are ionized at  $T = 300 \text{ K}$ . Thus, with a more correct description of the energy dispersions, one can better analyze the electron and hole dynamics in the  $\text{CuIn}_{1-x}\text{Ga}_x\text{Se}_2$  ( $x = 0, 0.5$ , and  $1$ ) alloys, thereby better understand the electrical properties of these compounds.

**III Dielectric function spectra at 40 K and critical-point energies for CuIn<sub>0.7</sub>Ga<sub>0.3</sub>Se<sub>2</sub>**  
S.G. Choi, R. Chen, C. Persson, T.J. Kim, S.Y. Hwang, Y. D. Kim, and L. M. Mansfield, *Appl. Phys. Lett.* **101**, 261903 (2012).

We have calculated the dielectric function spectra of CuIn<sub>0.5</sub>Ga<sub>0.5</sub>Se<sub>2</sub> by the all electron and full-potential linearized augmented plane wave (FPLAPW) method. The calculated dielectric function is compared with experimental values (CuIn<sub>0.7</sub>Ga<sub>0.3</sub>Se<sub>2</sub>) at temperature of 40 K and 300 K, and they are in a good agreement. The different contributions to imaginary part of dielectric function in terms of the transitions between the valence bands and the conduction bands are identified based on this calculation. Moreover, the  $\mathbf{k}$ -dependence of the interband critical points (CPs) along the main symmetry directions is analyzed as well.

# Chapter 5

## Concluding remarks and future work

Chalcopyrite copper indium gallium diselenide (CIGS) is seen as one of the most promising solar cell material for the near future. The maximum conversion efficiency of CIGS had reached 23.3% in the laboratory. In the current work, two major researches are analyzed. (1): Parameterization of energy bands for  $\text{CuIn}_{1-x}\text{Ga}_x\text{Se}_2$  where  $x = 0, 0.5$ , and  $1$ . With a more correct description of the energy dispersions, one can better analyze the electron and hole dynamics in the  $\text{CuIn}_{1-x}\text{Ga}_x\text{Se}_2$  ( $x = 0, 0.5$ , and  $1$ ) alloys, thereby better understand the electrical properties of these compounds. More importantly, this parameterization method can be utilized to other materials potentially. (2): The dielectric function spectra for the  $\text{CuIn}_{0.5}\text{Ga}_{0.5}\text{Se}_2$  is calculated by all electron and full-potential linearized augmented plane wave (FPLAPW) method, which is compared with experimental result. The probable electronic origins of the critical point features are discussed as well.

Alternative materials for solar cell are planning to be analyzed in the future work due to the cost and scarcity of indium in the CIGS. Copper zinc tin selenide (CZTSe) and copper zinc tin sulfide (CZTS) are also promising solar cell materials due to the low cost and non-toxicity elements in these compounds. It has many similarities with CIGS, such as similar device structure, fabrication techniques and tunable band gap. Therefore, it has huge potential for the future to reduce the cost of solar cells. Since the intensive research on those materials is relatively in a short time, therefore the conversion efficiency is only around 10% in the laboratory. Apparently, the quaternary chalcogenide semiconductor is more complicated compared with other thin film materials, more studies are needed in order to improve the conversion efficiency. This research should not be limited only within CZT(Se,S), other compounds are needed to be considered as well such as chalcogenide Cu-based compounds with transitional metals, such as CFT(Se,S). Also, it would be very useful to calculate conversion efficiency only based on the optical calculations based on DFT. Therefore, the model of conversion efficiency in multilayers solar cell device is planning to be calculated and analyzed in the future work as well.

# Acknowledgements

I would like to express my sincere appreciation to my supervisor Prof. Clas Persson for his academic encouragement and professional guidance. He is always showing a great interest to my projects and patient to teach me detailed material physics, which will be an invaluable asset to my future career.

I am grateful to Prof. Börje Johansson for the acceptance in his research group as a PhD student at KTH Royal Institute of Technology. I also thank Prof. Börje Johansson and Prof. Natalia Skorodumova for being my co-supervisor during my PhD study.

I appreciate Prof. Claudia Draxl to accept me visiting her group to learn Exciting Code at the University of Leoben in Austria and Humboldt University of Berlin in Germany, respectively. I also thank all the people who give me support and discuss with during my staying there.

I would like to thank all the group colleagues in Stockholm and Oslo for helpful research discussions and chatting: Alexander, Carlos, Dan, Fabiano, Girma, Gustavo, Hanyue, Kristian, Mathias, Maofeng, Mukesh, Priya, Roger, Sasha, Shen, Tiago. I also would like to thank Xuemei to help me arrange my apartment during staying in University of Oslo. I would like to thank all other people at the Department of Material Sciences and Engineering at KTH for creating a nice working atmosphere, especially for Huahai, Qiang and Song (names in alphabetical order).

The China Scholarship Council, the Swedish Energy Agency, and the Swedish Research Council, Stiftelsen Axel Hultgrens fond, Olle Erikssons stiftelse för materialteknik, and KTH Computational Science and Engineering Centre (KCSE) are acknowledged for financial support.

# Bibliography

- [1] <http://www.bp.com/>, 2014.
- [2] <http://www.iea.org/publications/scenariosandprojections/>, 2009.
- [3] G. P. Smestad. SPIE Press, 2002.
- [4] J. H. Seinfeld and S. N. Pandis. John Wiley & Sons, 2012.
- [5] G. Boyle. Oxford University Press, 2004.
- [6] D. Chiras. New Society Publishers, 2010.
- [7] <http://www.nrel.gov/ncpv/>, 2014.
- [8] H. Zhou, Q. Chen, G. Li, S. Luo, T.-B. Song, H.-S. Duan, Z. Hong, J. You, Y. Liu, and Y. Yang *Science*, vol. 345, p. 542, 2014.
- [9] F. Dimroth, M. Grave, P. Beutel, U. Fiedeler, C. Karcher, T. N. Tibbits, E. Oliva, G. Siefer, M. Schachtner, A. Wekkeli, *et al. Progress in Photovoltaics: Research and Applications*, vol. 22, p. 277, 2014.
- [10] R. Jones *Spectrolab, Inc. A Boeing Company. Sylmar, California, Estados Unidos*, 2009.
- [11] <http://www.gizmag.com/panasonic-hit-solar-cell-256-efficiency/31573/>, 2014.
- [12] J. S. Ward, B. Egaas, R. Noufi, M. Contreras, K. Ramanathan, C. Osterwald, and K. Emery in *Photovoltaic Specialist Conference (PVSC), 2014 IEEE 40th*, p. 2934, IEEE, 2014.
- [13] <http://www.zsw-bw.de/uploads/media/pr12-2014-ZSW-WorldrecordCIGS.pdf>, 2014.
- [14] M. A. Green, A. Ho-Baillie, and H. J. Snaith *Nature Photonics*, vol. 8, p. 506, 2014.
- [15] M. D. McGehee *Nature materials*, vol. 13, p. 845, 2014.

- [16] E. in Chief: Ali Sayigh. Elsevier Science, 2012.
- [17] A. Sproul *Solar Cells: Resource for the Secondary Science Teacher*, 2003.
- [18] D. A. Neamen and B. Pevzner. McGraw-Hill New York, 2003.
- [19] A. E. Becquerel *Comptes Rendus de l'Académie des Sciences*, vol. 9, p. 561, 1839.
- [20] L. Etgar *Materials*, vol. 6, p. 445, 2013.
- [21] G. Gourdin *Introduction to Green Chemistry Fall*, 2007.
- [22] R. S. Ohl, 03 1941.
- [23] R. S. Ohl, 05 1941.
- [24] S. Chen, X. Gong, A. Walsh, and S.-H. Wei *Physical Review B*, vol. 79, p. 165211, 2009.
- [25] S. Chen, X. Gong, A. Walsh, and S.-H. Wei *Applied Physics Letters*, vol. 94, p. 041903, 2009.
- [26] A. Walsh, S.-H. Wei, S. Chen, and X. Gong in *Photovoltaic Specialists Conference (PVSC), 2009 34th IEEE*, p. 001875, 2009.
- [27] C. Goodman *Journal of Physics and Chemistry of Solids*, vol. 6, p. 305, 1958.
- [28] B. Pamplin *Journal of Physics and Chemistry of Solids*, vol. 25, p. 675, 1964.
- [29] W. Hoffmann *Solar energy materials and solar cells*, vol. 90, p. 3285, 2006.
- [30] W. D. Brewer, R. Wengenmayr, and T. Bührke. John Wiley & Sons, 2013.
- [31] M. Cardona and Y. Y. Peter. Springer, 2005.
- [32] O. Madelung. Springer Berlin, 1996.
- [33] O. Madelung. Springer, 2004.
- [34] C. H. Henry *Journal of applied physics*, vol. 51, p. 4494, 1980.
- [35] W. Shockley and H. J. Queisser *Journal of applied physics*, vol. 32, p. 510, 1961.
- [36] Z. I. Alferov *Reviews of modern physics*, vol. 73, p. 767, 2001.
- [37] E. Yablonovitch, O. Miller, and S. Kurtz in *Photovoltaic Specialists Conference (PVSC), 2012 38th IEEE*, p. 001556, IEEE, 2012.
- [38] L. I. Maissel and R. Glang. McGraw-Hill New York, 1995.
- [39] D. E. Carlson and C. R. Wronski *Applied Physics Letters*, vol. 28, p. 671, 1976.

- [40] R. A. Street. Springer, 2000.
- [41] R. E. Schropp and M. Zeman. Kluwer Academic Boston, 1998.
- [42] [http://www.irena.org/DocumentDownloads/Publications/RE\\_Technologies\\_Cost\\_Analysis-SOLAR\\_PV.pdf](http://www.irena.org/DocumentDownloads/Publications/RE_Technologies_Cost_Analysis-SOLAR_PV.pdf), 2012.
- [43] C. A. Wolden, J. Kurtin, J. B. Baxter, I. Repins, S. E. Shaheen, J. T. Torvik, A. A. Rockett, V. M. Fthenakis, and E. S. Aydil *Journal of Vacuum Science & Technology A*, vol. 29, p. 030801, 2011.
- [44] P. V. Meyers *Solar Cells*, vol. 23, p. 59, 1988.
- [45] M. A. Green *Journal of Materials Science: Materials in Electronics*, vol. 18, p. 15, 2007.
- [46] P. Jackson, D. Hariskos, E. Lotter, S. Paetel, R. Wuerz, R. Menner, W. Wischmann, and M. Powalla *Progress in Photovoltaics: Research and Applications*, vol. 19, p. 894, 2011.
- [47] M. Kumar, H. Zhao, and C. Persson *Thin Solid Films*, vol. 535, p. 318, 2013.
- [48] R. Chen and C. Persson *Journal of Applied Physics*, vol. 112, p. 103708, 2012.
- [49] R. Chen and C. Persson *Thin Solid Films*, vol. 519, p. 7503, 2011.
- [50] C. Persson *Thin Solid Films*, vol. 517, p. 2374, 2009.
- [51] M. A. Green. Springer, 2006.
- [52] H. Hahn, G. Frank, W. Klingler, A.-D. Meyer, and G. Störger *Zeitschrift für anorganische und allgemeine Chemie*, vol. 271, p. 153, 1953.
- [53] S. Wagner, J. L. Shay, P. Migliorato, and H. M. Kasper *Applied Physics Letters*, vol. 25, p. 34, 1974.
- [54] C. Parlak and R. Eryiğit *Physical Review B*, vol. 73, p. 245217, 2006.
- [55] K. Hönes, M. Eickenberg, S. Siebentritt, and C. Persson *Applied physics letters*, vol. 93, p. 092102, 2008.
- [56] C. Persson *Applied Physics Letters*, vol. 93, p. 072106, 2008.
- [57] Z. B. Li *Advanced Materials Research*, vol. 239, p. 1304, 2011.
- [58] A. Luque and S. Hegedus. John Wiley & Sons, 2011.
- [59] C.-S. Jiang, R. Noufi, K. Ramanathan, J. AbuShama, H. Moutinho, and M. Al-Jassim *Applied physics letters*, vol. 85, p. 2625, 2004.
- [60] U. Rau and S. Siebentritt. Springer, 2006.

- [61] S. Chen, J.-H. Yang, X. Gong, A. Walsh, and S.-H. Wei *Physical Review B*, vol. 81, p. 245204, 2010.
- [62] S. Schuler, S. Siebentritt, S. Nishiwaki, N. Rega, J. Beckmann, S. Brehme, and M. C. Lux-Steiner *Physical review B*, vol. 69, p. 045210, 2004.
- [63] S. Lany and A. Zunger *Physical review letters*, vol. 100, p. 016401, 2008.
- [64] S. Zhang, S.-H. Wei, A. Zunger, and H. Katayama-Yoshida *Physical Review B*, vol. 57, p. 9642, 1998.
- [65] O. Madelung, U. Rössler, and M. Schulz. Springer, 2010.
- [66] H. Neumann *Solar Cells*, vol. 16, p. 317, 1986.
- [67] C. Persson, Y.-J. Zhao, S. Lany, and A. Zunger *Physical Review B*, vol. 72, p. 035211, 2005.
- [68] Y.-J. Zhao, C. Persson, S. Lany, and A. Zunger *Applied physics letters*, vol. 85, p. 5860, 2004.
- [69] O. Lundberg, M. Edoff, and L. Stolt *Thin Solid Films*, vol. 480, p. 520, 2005.
- [70] O. Lundberg, J. Lu, A. Rockett, M. Edoff, and L. Stolt *Journal of Physics and Chemistry of Solids*, vol. 64, p. 1499, 2003.
- [71] K. Ramanathan, M. A. Contreras, C. L. Perkins, S. Asher, F. S. Hasoon, J. Keane, D. Young, M. Romero, W. Metzger, R. Noufi, et al. *Progress in Photovoltaics: Research and Applications*, vol. 11, p. 225, 2003.
- [72] K. H. Kim, K. C. Park, and D. Y. Ma *Journal of Applied Physics*, vol. 81, p. 7764, 1997.
- [73] T. Minami, H. Nanto, and S. Takata *Japanese Journal of Applied Physics*, vol. 23, p. L280, 1984.
- [74] N. Naghavi, D. Abou-Ras, N. Allsop, N. Barreau, S. Bücheler, A. Ennaoui, C.-H. Fischer, C. Guillen, D. Hariskos, J. Herrero, et al. *Progress in Photovoltaics: Research and Applications*, vol. 18, p. 411, 2010.
- [75] S. Niki, M. Contreras, I. Repins, M. Powalla, K. Kushiya, S. Ishizuka, and K. Matsubara *Progress in Photovoltaics: Research and Applications*, vol. 18, p. 453, 2010.
- [76] J. Kessler, M. Bodegård, J. Hedström, and L. Stolt *Solar energy materials and solar cells*, vol. 67, p. 67, 2001.
- [77] R. M. Martin. Cambridge University Press, 2004.
- [78] R. M. Martin. freely available <http://www.wien2k.at/reg user/textbooks>, 2013.

- [79] M. Born and J. R. Oppenheimer *Annalen der Physik (Leipzig)*, vol. 84, p. 457, 1927.
- [80] D. R. Hartree *Proceedings of the Royal Society of London*, vol. A113, p. 621, 1928.
- [81] V. Fock *Zeitschrift für Physik*, vol. 61, pp. 126–148, 1930.
- [82] P. Hohenberg and W. Kohn *Physical review*, vol. 136, p. B864, 1964.
- [83] W. Kohn and L. J. Sham *Physical Review*, vol. 140, p. A1133, 1965.
- [84] C. Persson. Lecture notes, 2013.
- [85] D. P. Bertsekas, A. Nedić, and A. E. Ozdaglar. Athena Scientific Belmont, 2003.
- [86] J. C. Slater *Physical Review*, vol. 81, p. 385, 1951.
- [87] U. von Barth and L. Hedin *Journal of Physics C: Solid State Physics*, vol. 5, p. 1629, 1972.
- [88] L. Hedin and B. Lundqvist *Journal of Physics C: Solid state physics*, vol. 4, p. 2064, 1971.
- [89] D. J. Tozer and N. C. Handy *The Journal of chemical physics*, vol. 108, p. 2545, 1998.
- [90] F. A. Hamprecht, A. J. Cohen, D. J. Tozer, and N. C. Handy *The Journal of chemical physics*, vol. 109, p. 6264, 1998.
- [91] T. Grabo and E. K. Gross *Chemical physics letters*, vol. 240, p. 141, 1995.
- [92] A. J. Cohen, P. Mori-Sánchez, and W. Yang *The Journal of chemical physics*, vol. 126, p. 191109, 2007.
- [93] C. Kittel and P. McEuen. Wiley New York, 1976.
- [94] J. Slater *Physical Review*, vol. 51, p. 846, 1937.
- [95] T. L. Loucks. W.A. Benjamin, Inc., 1967.
- [96] O. K. Andersen *Physical Review B*, vol. 12, p. 3060, 1975.
- [97] D. Koelling and G. Arbman *Journal of Physics F: Metal Physics*, vol. 5, p. 2041, 1975.
- [98] D. Singh *Physical Review B*, vol. 43, p. 6388, 1991.
- [99] E. Sjöstedt, L. Nordström, and D. Singh *Solid state communications*, vol. 114, p. 15, 2000.
- [100] L. Nordstrom and D. J. Singh. Springer, 2006.

- [101] A. Gulans, S. Kontur, C. Meisenbichler, D. Nabok, P. Pavone, S. Rigamonti, S. Sagmeister, U. Werner, and C. Draxl *Journal of Physics: Condensed Matter*, vol. 26, p. 363202, 2014.
- [102] D. R. Penn *Physical Review*, vol. 128, p. 2093, 1962.
- [103] M. Fox and G. F. Bertsch *American Journal of Physics*, vol. 70, p. 1269, 2002.
- [104] C. Ambrosch-Draxl and J. O. Sofo *Computer Physics Communications*, vol. 175, p. 1, 2006.
- [105] L. C. L. Y. Voon and M. Willatzen. Springer, 2009.
- [106] E. Kane *Semiconductors and Semimetals*, vol. 1, p. 75, 1966.
- [107] C. Persson and C. Ambrosch-Draxl *Computer physics communications*, vol. 177, p. 280, 2007.
- [108] B. Thaller. Springer-Verlag Berlin, 1992.
- [109] P. A. M. Dirac. The Clarendon Press, 1930.
- [110] E. van Lenthe, E.-J. Baerends, and J. G. Snijders *The Journal of chemical physics*, vol. 101, p. 9783, 1994.
- [111] S. Faas, J. Snijders, J. Van Lenthe, E. Van Lenthe, and E. Baerends *Chemical physics letters*, vol. 246, p. 632, 1995.
- [112] E. Van Lenthe, J. Snijders, and E. Baerends *The Journal of chemical physics*, vol. 105, p. 6505, 1996.
- [113] S. Siebentritt, M. Igalson, C. Persson, and S. Lany *Progress in Photovoltaics: Research and Applications*, vol. 18, p. 390, 2010.
- [114] K.-H. Hellwege and L. C. Green *American Journal of Physics*, vol. 35, p. 291, 1967.